Theory of Wave Formation in Liquid Metal

Kevin Brannick

Thesis submitted to the Faculty of the
Virginia Polytechnic Institute and State University
in partial fulfillment of the requirements for the degree of

Master of Science
in
Aerospace Engineering

Bhuvana Srinivasan, Chair
Stefano Brizzolara
Colin Adams

January 7, 2022
Blacksburg, Virginia

Keywords: Magnetohydrodynamic, Z-pinch, Liquid Metal

Theory of Wave Formation in Liquid Metal

Kevin Brannick

ABSTRACT

The analytical solution presented in this thesis is based on the Liquid Metal Experiment (LEX) at Virginia Tech to determine the practicality of replacing a solid metal electrode with a liquid metal electrode wall. Replacing the solid metal with a liquid metal may improve the operational lifetime of Z-pinches. The LEX is based upon the University of Washington's High Energy Density Z-pinch (ZaP-HD) and Fusion Z-Pinch Experiments (FuZE) and replaces one solid metal electrode with a liquid metal electrode. During the operation of the ZaP-HD and FuZE, a plasma column exerts electromagnetic forces and pressure on a solid electrode wall. The pressure exerted by the plasma column is called the magnetic pressure. In the Virginia Tech device magnetic pressure is exerted by a wire onto the liquid metal electrode. The magnetic pressure in the LEX displaces the liquid metal electrode free surface, and subsequently creates a waveform. The initial free surface displacement and subsequent wave motion of the liquid metal is found by analyzing the geometry of the device, the electromagnetic forces generated during operation, and material properties of the tin-bismuth liquid metal mixture. The initial displacement for changing current, current pulse length, tin percentage, and applied pressure range are investigated. The results are compared for verification and validation. These methods are shown to be accurate to within an order of magnitude and are valid for an axisymmetric domain. The results presented here may inform further experimentation and aid in improving designs for newer devices.

Theory of Wave Formation in Liquid Metal

Kevin Brannick

GENERAL AUDIENCE ABSTRACT

This thesis presents analytical solutions for creating waveforms in liquid metal due to electromagnetic forces. The motivation for developing the analytical solutions is to aid in developing a device created by Virginia Polytechnic and State University (Virginia Tech). The Liquid Metal Experiment (LEX) at Virginia Tech investigates the practicality of incorporating a liquid metal into a Z-pinch fusion device under development at the University of Washington's High Energy Density Z-pinch (ZaP-HD) and Fusion Z-Pinch Experiments (FuZE). The ZaP-HD and FuZE experiments are cylindrical and aim to investigate the viability of Z-pinches as fusion devices. An electric current passes between an internal electrode, the plasma column, and an external electrode along the z-axis of the Z-pinch. The time duration of the current is typically on the order of tens of microseconds. The plasma column and subsequent fusion events are generated only during this duration. During this duration, the interactions between the plasma column and the electrodes cause the electrodes to deteriorate. In standard Z-pinch devices, the electrodes are solid metal and deteriorate during the operation, limiting the device's lifespan. The liquid metal introduces other complexities to the system. During the time duration of the current, the electromagnetic forces produce a pressure gradient at the free surface of the liquid metal. The pressure created by the electromagnetic forces generates waveforms within the liquid metal. The analytical solutions presented in this thesis include electrodynamic solutions to find the pressure, kinematic solutions to determine the free surface displacement of the liquid metal due to the pressure, and fluid dynamic solutions of the waveform caused by the initial free surface displacement.

Acknowledgments

This work was partially supported by the Department of Energy ARPA-E BETHE program under grant number DE-AR0001263.

Contents

List of Figures

List of Tables

List of Abbreviations

α	Dispersion Relation
χ	Volumetric Magnetic Susceptibility
ϵ	Absolute Permittivity Constant
ϵ_o	Permittivity Constant
ϵ_r	Relative Permeability
η	Free Surface Elevation
η_0	Initial Free Surface Elevation
$_0$	Bessel Function
$\mathbf{B}$	Magnetic Field
$\mathbf{j}$	Current Density
$\mathbf{v}$	Velocity
μ	Absolute Permeability Constant
μ_o	Permeability Constant
∇P	Pressure Gradient
ω	Frequency
ϕ	Velocity Potential

ρ	Density
σ	Conductivity
b	Applied Pressure Range
F_{ext}	Force Exerted
g	Gravity
h	Depth of Liquid Metal
I_0	Current Amplitude
m_a	Accelerated Mass
P	Pressure
P_{CD}	Current Density Pressure
P_{mag}	Magnetic Pressure
r	Radius
t_0	Current Duration
Z	Initial Free Surface Displacement Magnitude
CFD	Computational Fluid Dynamics
d	Skin Depth
FuZE	Fusion Z-Pinch Experiment
MHD	Magneto Hydro Dynamics
ZaP-HD	University of Washington's High Energy Density Experiment

Chapter 1

Introduction

This chapter provides background information and motivations for developing the analytical solutions. The analytical solutions describe the creation of an initial displacement and subsequent waveform in liquid metal due to an imparted pressure. The pressure in this solution comes from electromagnetic forces. The electromagnetic forces generated in the Liquid Metal Experiment (LEX) at Virginia Tech mimic the electromagnetic forces in the University of Washington's High Energy Density Z-pinch (ZaP-HD) and Fusion Z-Pinch Experiments (FuZE). Z-pinch devices have been explored to advance fusion energy research. The specific energy of fusion fuels is one of the main motivations for fusion energy research. The specific energy of various fusion, fission, chemical, and electro-chemical reaction are discussed in this chapter.

Plasma is often described as the fourth state of matter, or simply as ionized gas. A more accurate definition is "A plasma is a quasineutral gas of charged and neutral particles that exhibits a collective behavior." Chen, "An Introduction to Plasma and Controlled Fusion" [7].

Within the plasma, the constituent particles are free to move in all directions, similar to a gas. In the absence of electric and magnetic fields the free motion is in all directions. The range of motion is further complicated by the Coulomb forces active between each of the charged particles within the plasma region. The range of the Coulomb force between two charged particles diminishes as $1/r^2$, as in Equation 1.1.

$$F_e = k\frac{|g_1||q_2|}{r^2} \tag{1.1}$$

The moving particles then constitute an electric current, which generates a magnetic field, shown in Figure 1.1. Fusion events can occur in compressed plasmas or those confined by electromagnetic forces. The compression of the plasma increases the density of the plasma. As the density of the plasma increases so does the rate at which the ions overcome the repulsive forces between each other and fuse. The relative movement of charged particles constitutes an electric current. An electric current between two points in a line generates an azimuthal magnetic field, as in Figure 1.1. An increase in the electric field in the plasma, increases the electric current. An increase in the azimuthal magnetic field constricts the plasma in proportion to the square of the magnetic field strength. The greater the magnetic field the more compressed the plasma becomes.

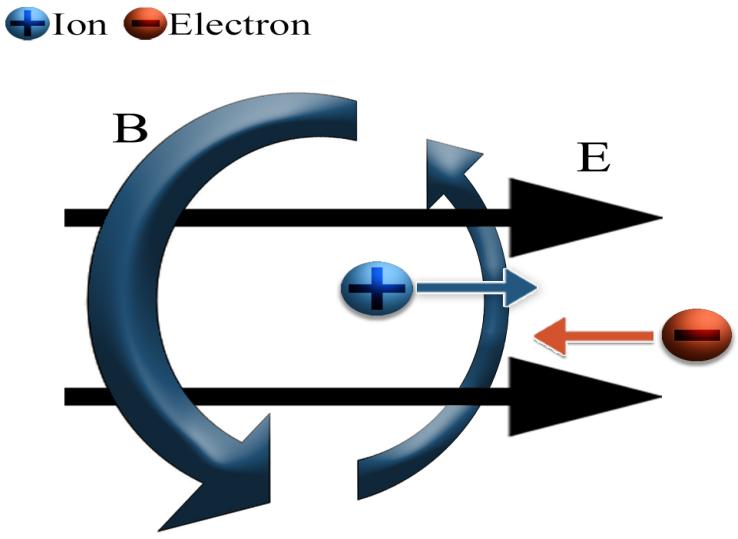

Figure 1.1: Ions and electrons move along the electric field lines generating a magnetic field. Increasing the electric field increases the speed of the ions and electrons. The increase in speed of the ions and electrons increases the strength of the magnetic field. As the magnetic field strength increases the more compressed the ions become. The electrons move faster than the ions and are responsible for the creation of the magnetic field.

1.1 Background on Fusion and Z-Pinches

Nuclear fusion is a subject of research, due to its high energy density relative to other fuel sources. Table 1.1 shows the relative energy densities of common reaction types used for fuel generation and storage. The specific energy of both fusion and fission nuclear reaction are orders of magnitude greater than common chemical reactions. The chemical and nuclear stoichiometry calculations of energy density for fusion, fission, and methane are provided in Appendix **??**. Electro-chemical reactions have the lowest specific energy of the three reaction types. Electro-chemical reactions are used for batteries and other methods of storing energy. Chemical reactions have specific energies two orders of magnitude higher than electro-chemical reactions. Chemical reactions are used for most of the world's energy production. The availability of chemical fuel sources is limited, and nuclear alternatives are viable long-term replacements. Nuclear reactions have specific energies of higher magnitude than chemical reactions. Fission is the only commercial nuclear power source currently available. One of the negative aspects of nuclear fission is that the waste material is radioactive. Most of the waste material remains radioactive for hundreds to thousands of years after it has been used [18]. Nuclear fusion has a higher specific energy than fission. Components of fusion reactors still become radioactive over time. However, the radioactive components remain radioactive for decades, rather than centuries. The higher specific energy and the shorter radioactive half-life of nuclear fusion are motivations for pursuing a commercially viable fusion reactor.

The Z-pinch is a promising potential option for creating a commercially operational fusion reactor. The Z-pinch utilizes a simple, compact design to achieve fusion. Figure 1.2 is a diagram of the Z-pinch device being developed at ZaP-HD and FuZE. In this design, current is passed from exterior to interior electrode through the plasma along the z-axis. The azimuthal magnetic field constricts the plasma to the point where fusion occurs. The

Table 1.1: Energy densities for Nuclear, Chemical, and Electro-chemical Reactions

Reaction Type	Fuel Material	Specific Energy [MJ/kg]
Nuclear	Fusion Deuterium-Tritium	3.37×10^{8}
	Fission Uranium	8.06×10^{7}
Chemical	Methane	54
	Wood	18
Electro-chemical	Lithium-ion	0.36-0.875
	Lead-acid	0.17

main components of the device are the inner electrode, the outer electrode, the neutral gas injector, and the electrode end wall. Replacing the electrode end wall with a liquid metal is the motivation for the LEX and the analytical solutions.

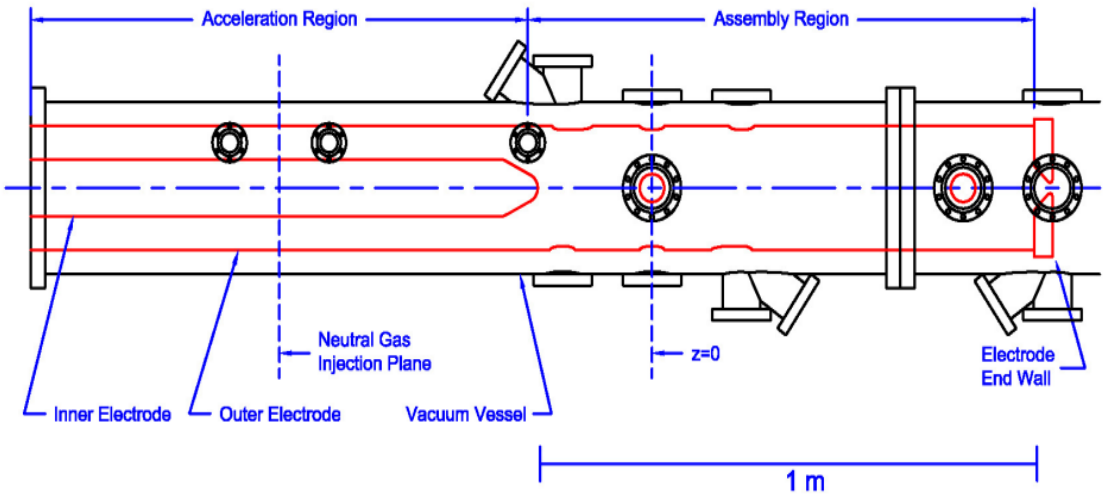

Figure 1.2: Schematic of the ZaP-HD Z-pinch. The inner electrode is on the left and the electrode end wall is on the right. Neutral gas injection occurs in the acceleration region on the left. The plasma column is formed in the assembly region between the inner electrode and the electrode end wall. Sheared Flow Stabilized Z-Pinch University of Washington [14].

Figure 1.3 shows the steps by which fusion may be achieved. During steps t_1 to t_2, neutral gas is injected into the acceleration region. During this time, the circuit between the inner and outer electrode is open. At time t_3, enough neutral gas is injected into the acceleration

region, and the circuit closes. At this time, the current released by the capacitor bank passes from the outer electrode to the inner electrode through the neutral gas. The neutral gas becomes ionized, creating plasma. A coaxial electric current forms within the plasma. The coaxial electric current generates an azimuthal magnetic field. The azimuthal magnetic field compresses the plasma region. Due to Lorentz forces, the plasma accelerates towards the assembly region. The azimuthal magnetic field continues to narrow the plasma during time t_5 until time t_6. At time t_6, the plasma has reached the electrode end wall. When the plasma has reached the electrode end wall, the current travels from the outer to the inner electrode through the plasma along the Z-axis. Hence, the name Z-pinch. The Z-pinch achieves fusion during the time t_6 due to the axial current generating the azimuthal magnetic field. The azimuthal magnetic field radially compresses the plasma and has the potential to produce fusion events.

Thermal stresses, between the plasma and the electrode end wall, cause the end wall to deteriorate. The deterioration of the electrode end wall is a hindrance to the operational lifespan of the device. A liquid metal electrode end wall has the potential to mitigate the deterioration and increase the operational lifespan of Z-pinch devices. The introduction of the liquid metal end wall presents additional complexities to the system. The current that constricts the plasma column results in a magnetic pressure onto the liquid metal free surface. The pressure displaces the liquid metal and creates waves that travel outward from the plasma column.

1.2 Objectives

This thesis presents the development of an analytical solution for waves in liquid metals caused by electromagnetic forces. The analytical solution is based on the LEX to determine

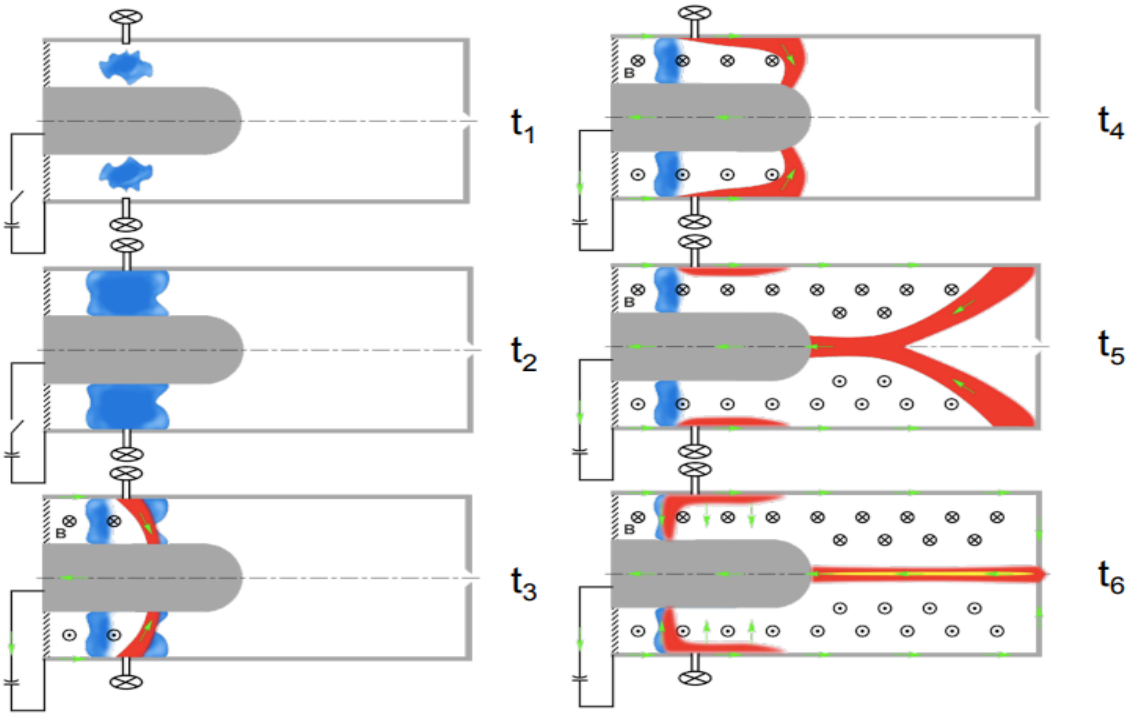

Figure 1.3: Time-lapse of Z-pinch plasma column generation. Between t_1 and t_2 neutral gas is injected. Between t_3 and t_4 the plasma is accelerated towards the electrode end wall. Between t_5 and t_6 the plasma column forms. Sheared Flow Stabilized Z-Pinch University of Washington [14].

the practicality of replacing the solid metal wall electrode with a liquid metal wall electrode. The device mimics the Z-pinch configuration by exchanging the plasma column with a solid wire. This wire completes the circuit and creates the same electromagnetic geometry as the plasma column. The electromagnetic geometry produces magnetic pressure, which displaces the liquid metal electrode. The analytical solutions find the free surface displacement of the liquid metal and the resulting waveform. This thesis presents two methods for calculating the initial free surface displacement. One method for calculating the initial displacement uses the magnetic pressure. The other method uses the current density within the liquid metal. In Chapter 5 both methods are compared to a full computational fluid dynamics solver.

This is a continuation of work presented by Lokenath Debnath in Nonlinear Water Waves [2]. Lokenath Debnath's solutions for a pressure pulse in an axisymmetric Cauchy-Poisson problem is used as the foundation for the fluid dynamic portion of the analytical solution. Chapter 2 details the solutions for the magnitude and shape of the pressure.

Chapter 2

Electrodynamics Formulation

This chapter develops the electrodynamic and kinematic equations. The electrodynamic and kinematic equations determine the initial displacement of the liquid metal. This chapter also details the general configuration of both the LEX and the analytical solution. This includes the coordinate system used, physical dimensions of the liquid metal, and the physical dimensions of the device. The electrodynamic formulation begins by approximating the current passing through the wire (from experimental data) and determining the resultant magnetic field. The magnetic field impacts the two methods for finding the pressure applied to the liquid metal surface. The first method utilizes the magnetic pressure to find the displacement. The second method utilizes the current density within the liquid metal. Both methods calculate the pressures for the entire free surface of the liquid metal. The kinematic equation uses averaged pressure values to determine the initial free surface displacement.

2.1 Device and Analytical Solution Configuration

Figure 2.1 shows the LEX. The LEX's interior and exterior coaxial electrodes are vertically aligned, in contrast to the ZaP-HD and FuZE experiments, horizontal alignment in Figure 1.2. The vertical alignment allows for the liquid metal electrode wall to pool and form at the bottom of the device. Figure 2.2 shows the liquid metal electrode wall. Figure 2.2 also shows the wire that mimics the plasma column in the ZaP-HD and FuZE experiments.

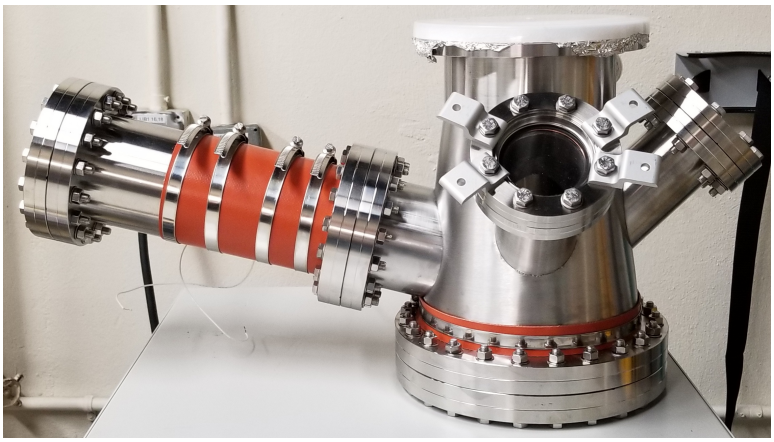

Figure 2.1: External image of the LEX [1]

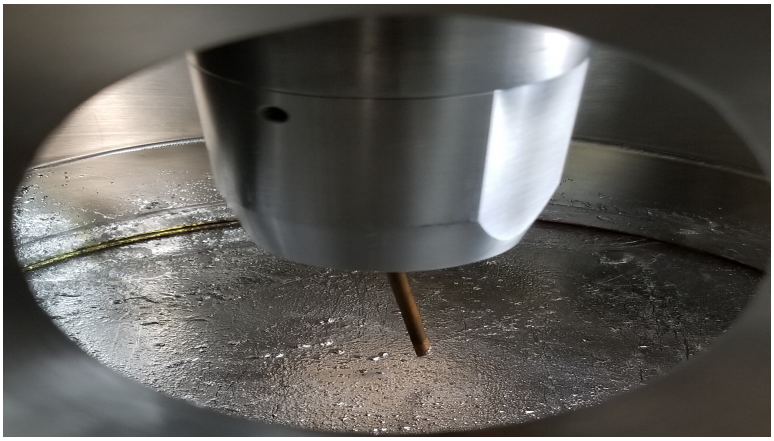

Figure 2.2: Internal image of the LEX. The liquid metal and the wire are shown [1].

Figure 2.3 shows a cross section of the LEX. The exterior electrode is dark grey. The liquid metal electrode wall is blue. The wire is brown and partially submerged into the liquid metal. The interior electrode is light grey.

The analytical solutions incorporate the cylindrical coordinate system shown in Figure 2.4. The z-axis is coaxial with the wire. The r-axis extends radially from the center to exterior electrode, parallel to the liquid metal surface. The azimuthal, θ, angle revolves around the z-axis.

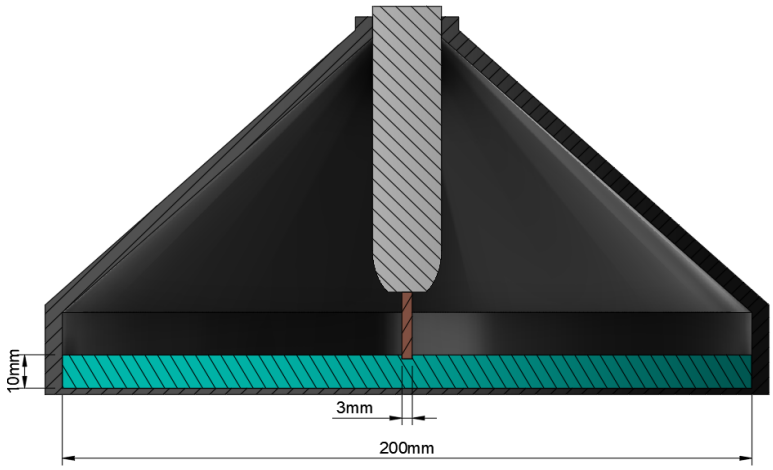

Figure 2.3: Cross-section of the LEX. The exterior electrode is dark grey. The liquid metal electrode wall is blue. The wire is brown and partially submerged into the liquid metal. The interior electrode is light grey.

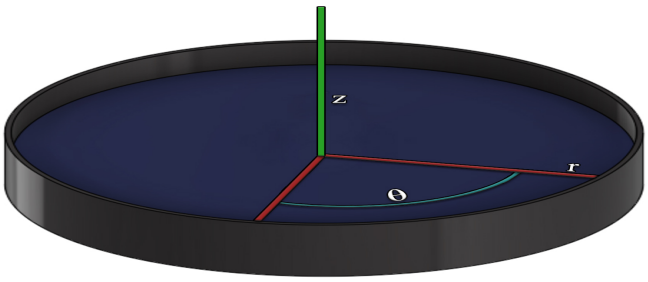

Figure 2.4: The coordinate system of the LEX used in the analytical solutions. The z-axis is coaxial with the wire. The r-axis is parallel to the liquid metal surface. The θ-axis is azimuthal in reference to the zero point of the r-axis.

2.2 Current Flow

A capacitor bank supplies the current to the wire. The choice of current amplitude impacts both the magnetic field. The current flows down the wire from the capacitor bank into the liquid metal. The liquid metal then acts as an electrode, carrying the current to the interior surface of the outer chamber wall, completing the circuit. This thesis approximates

the current as a square wave pulse with a fixed current amplitude, I_0, and frequency, ω. Figure 2.5 shows the benchmark data along with the approximations used in this thesis. The benchmark data is generated by a circuit model developed in the planning phase of the LEX. The circuit model predicts the magnitude of the current and the time period it is deposited into the liquid metal.

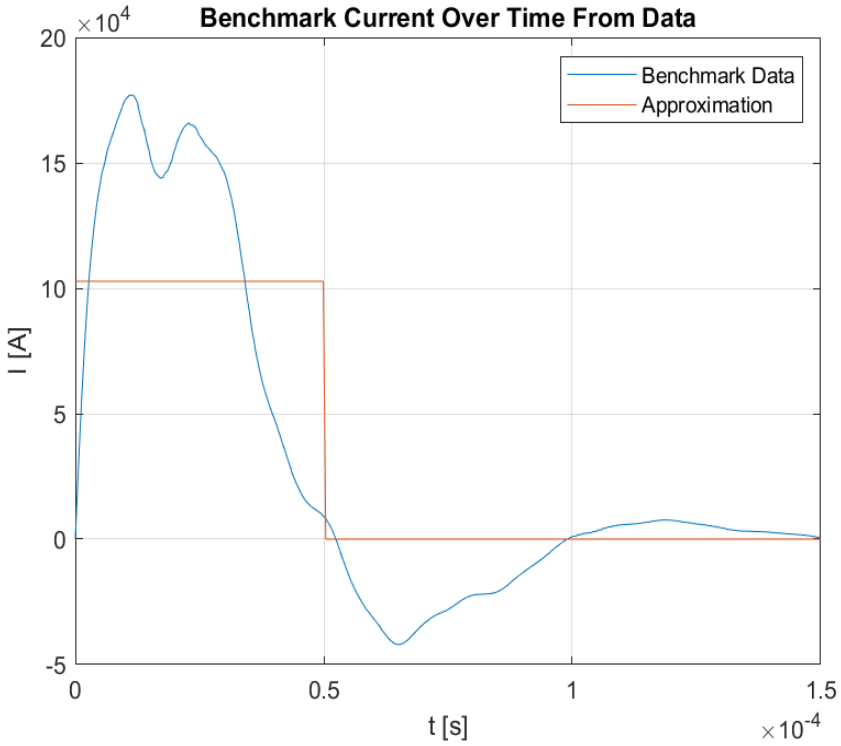

Figure 2.5: Experimental and approximated current over time. The blue line is the experimental current and the red line is the approximated current. The approximated current is the average of the experimental current data during the first 50 microseconds.

The approximated current is 100 kiloamperes over 50 microseconds. In Figure 2.5, the red line represents the approximation, and the blue line represents the experimental data. This thesis uses the square wave approximation in Figure 2.5. In Figure 2.5, the negative values beyond the 50-microsecond mark represents a reversal of the current after the initial current has been supplied, due to underdamped ringing of the energizing circuit.

The current self-consistently produces a magnetic field everywhere that it is on the liquid metal surface, the current flows radially. The radial current in the liquid metal and the azimuthal magnetic field at the interface produce a pressure gradient at the liquid metal surface.

2.3 Magnetic Field

The strength of the magnetic field inside the wire increases until it reaches the radius of the wire, where it then quickly decreases. The electric current in the wire produces the azimuthal magnetic field. Ampére's law relates the magnetic field in two regions to the electric current. The first region is inside the wire, and the second is outside of the wire. Ampére's circuital law in integral form is

$$\oint_C \mathbf{B} \cdot \ d\mathbf{l} = \mu_0 \iint_S \mathbf{j}_{wire} \cdot d\mathbf{A}. \tag{2.1}$$

The left-hand-side of Equation 2.1 represents the integral of the magnetic field around a loop and the right-hand-side represents the current traveling through the cross-sectional area of the loop. Due to the current only flowing in the $\hat{z}$-direction of the wire, the magnetic field produced by the wire will only have an azimuthal (θ) component.

Equation 2.2 is the current density of the wire.

$$\mathbf{j}_{wire} = -\frac{I_0}{2\pi R_{wire}^2}\hat{z}\left[\frac{A}{m^2}\right] \tag{2.2}$$

In Equation 2.2 the wire only has a negative $\hat{z}$ component. The negative sign on the current density, $\mathbf{j}_{wire}$, results in the magnetic field created only having a negative $\hat{\theta}$ component.

Using this current density, the magnetic field in units of tesla inside, $r < R_{wire}$, and outside, $r > R_{wire}$. Equation 2.3 finds the magnetic field within the wire.

$$\begin{aligned}
\oint_C \mathbf{B} \cdot \ d\mathbf{l} &= \mu_0 \iint_S \mathbf{j}_{wire} \cdot d\mathbf{A}, \quad r < R_{wire} \\
\mathbf{B} 2\pi r &= \mu_0 \iint_S \frac{-I_0}{2\pi R_{wire}^2} \cdot d\mathbf{A}, \quad r < R_{wire} \\
\mathbf{B} 2\pi r &= \mu_0 \left(\frac{-I_0}{2\pi R_{wire}^2} \right) 2\pi r^2, \quad r < R_{wire} \\
\mathbf{B}(r) &= -\left(\frac{\mu_0 I_0}{2\pi R_{wire}^2} \right) r \ \ \hat{\theta} \ \ [T], \quad r < R_{wire}
\end{aligned} \tag{2.3}$$

Equation 2.4 finds the magnetic field outside the wire.

$$\begin{aligned}
\oint_C \mathbf{B} \cdot \ d\mathbf{l} &= \mu_0 \iint_S \mathbf{j}_{wire} \cdot d\mathbf{A}, \quad r > R_{wire} \\
\mathbf{B} 2\pi r &= \mu_0 \iint_S \frac{-I_0}{2\pi R_{wire}^2} \cdot d\mathbf{A}, \quad r > R_{wire} \\
\mathbf{B} 2\pi r &= \mu_0 \left(\frac{-I_0}{2\pi R_{wire}^2} \right) 2\pi R_{wire}^2, \quad r > R_{wire} \\
\mathbf{B}(r) &= -\frac{\mu_0 I_0}{2\pi r} \ \ \hat{\theta} \ \ [T], \quad r > R_{wire}.
\end{aligned} \tag{2.4}$$

Thus, the current in the wire, I_0, generates a magnetic field above the liquid metal in two regions; one within, the other external to the radius of the wire.

$$\mathbf{B}(r) = \begin{cases} -\left(\frac{\mu_0 I_0}{2\pi R_{wire}^2} \right) r \ \ \hat{\theta} \ \ [T], & r < R_{wire} \\ -\frac{\mu_0 I_0}{2\pi r} \ \ \hat{\theta} \ \ [T], & r > R_{wire} \end{cases} \tag{2.5}$$

Figure 2.6 shows the magnetic field.

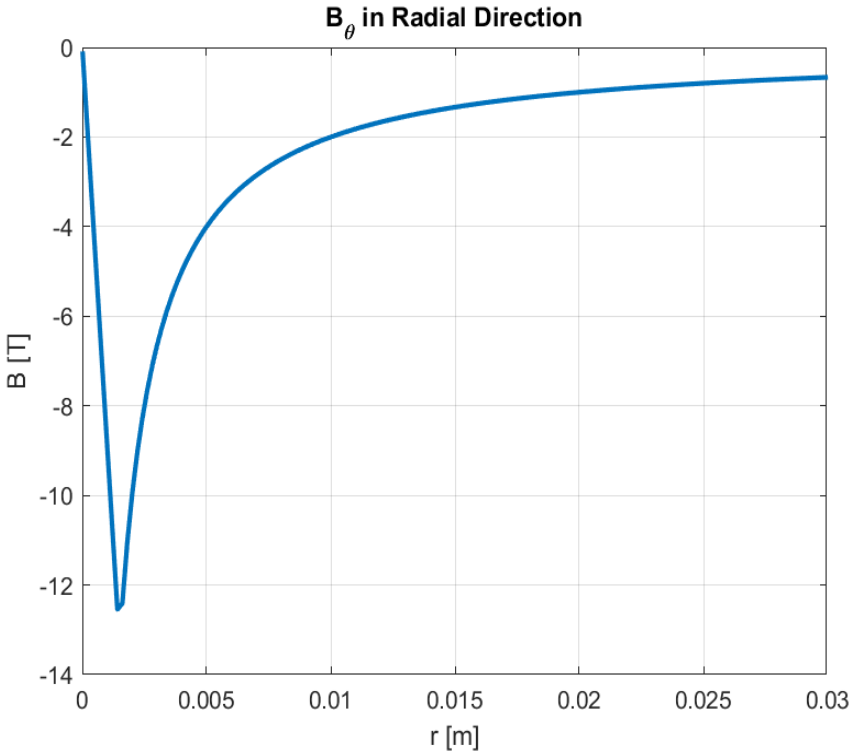

Figure 2.6: Variation in the azimuthal magnetic field strength with radius. The magnitude of the magnetic field strength is greatest at the radius of the wire.

2.4 Pressure

To calculate the pressure applied to the liquid metal free surface we begin with the magneto-hydrodynamic (MHD) momentum equation, Equation 2.6. The density is ρ, velocity is $\mathbf{v}$, pressure is P, the current density is $\mathbf{j}$, the magnetic field is $\mathbf{B}$, and gravity is $\mathbf{g}$.

$$\rho\frac{\partial \mathbf{v}}{\partial t} + \rho(\mathbf{v}\times\nabla)\mathbf{v} = -\nabla P + \mathbf{j}\times\mathbf{B} + \rho\mathbf{g} \tag{2.6}$$

Equation 2.6 is simplified by ignoring resistance and gravity.

$$\rho\frac{\partial \mathbf{v}}{\partial t} = -\nabla P + \mathbf{j}\times\mathbf{B} \tag{2.7}$$

The steady case simplifies to

$$\nabla P = \mathbf{j} \times \mathbf{B}. \tag{2.8}$$

The equilibrium momentum Equation 2.8 may be used to find the pressure after the current density is known. Section 2.5 through Section 2.7 finds the pressure applied to the liquid metal free surface using only the current density. This method involves approximations for skin depth and the path of the current through the liquid metal.

The other method for finding the pressure is by calculating the magnetic pressure. Equation 2.8 and Maxwell's equation 2.9 are combined to find the magnetic pressure, Equation 2.11

$$\mu_0 \mathbf{j} = \nabla \times \mathbf{B} \tag{2.9}$$

$$\nabla P = -\frac{1}{2\mu_0} \nabla B^2 \tag{2.10}$$

$$P = -\frac{1}{2\mu_0} B^2 \tag{2.11}$$

Equation 2.11 is dependent only on the magnetic field. Section 2.9 details the difference in initial free surface displacement between magnetic pressure and current density methods.

2.5 Skin Depth

The way in which the wire deposits the current into the liquid metal is of particular importance, as it dictates the distribution of the current density. The current ceases to flow in a simple linear direction, such as in the wire, and instead gains a radial component. This

causes the linear current to become dependent on both the r and z directions. The current density's $\hat{z}$ dependence is an exponential decay that depends on the skin depth of the liquid metal. The radial component of the liquid metal current density is dependent on the z position.

The skin depth is the measure of how the current dissipates through the metal. It is dependent upon three physical characteristics of the metal. The volumetric magnetic susceptibility, χ, the conductivity, σ, and the relative permeability, ϵ_r. The metals used in that experiment are tin and bismuth. The skin depth is found by Equation 2.12

$$d = \left[\omega \left(\frac{\epsilon\mu}{2}\right)^{1/2} \left(\sqrt{1 + \left(\frac{\sigma}{\epsilon\omega}\right)^2} - 1\right)^{1/2}\right]^{-1} \text{[m]}. \tag{2.12}$$

In Equation 2.12, ω is the frequency of the current discharge, ϵ is the absolute permittivity, μ is the absolute permeability, and σ is the conductivity. Table 2.1 presents the values of these terms used in the calculation of current density. In the current density method, there are two ways in which the skin depth impacts the initial free surface displacement of the liquid metal. The first is that it determines how the magnitude of the current density decreases with increasing depth. The second is that it affects how the range of depth over which the pressure gradient is applied in the calculation of the pressure. The absolute permittivity, ϵ, the absolute permeability, μ, and the conductivity values are dependent on which liquid metal is used. The permittivity of a material is a measure of its electric polarizability. This is a measure of how the material responds when exposed to an electric field. Equation 2.13 expresses the absolute permittivity.

$$\epsilon = \epsilon_0 \epsilon_r \quad \left[\frac{F}{m}\right]. \tag{2.13}$$

The same is not true for the absolute permeability μ. Equation 2.14 expresses the absolute permeability in terms of the permeability of free space and the magnetic susceptibility. Volumetric magnetic susceptibility, χ, is the measure of how magnetized a material will become when exposed to a magnetic field.

$$\mu = \mu_0(\chi + 1) \left[\frac{\text{H}}{\text{m}}\right] \tag{2.14}$$

The last value needed for the calculation of skin depth is the conductivity, σ, of the liquid metal. The value of conductivity is intrinsic to the material and is a function of temperature. The liquid metal is a tin and bismuth alloy. The values used in the calculations are

Table 2.1: Material constants and averaged values

Material	χ	μ [H m^{-1}]	σ [Ω]	ϵ_r	ϵ [F m^{-1}]	ρ [kg m^{-3}]
Tin	-2.27E-5	1.257E-6	9.10E6	1	8.85E-12	6,990
Bismuth	-1.70E-4	1.254E-6	7.70E5	1	8.85E-12	10,050
Averaged	-1.70E-4	1.266E-6	7.70E5	1	8.85E-12	8,520

approximations found with a simple average of the two values.

The skin depth is

$$d = 4.0 \times 10^{-3} \ \ [\text{m}], \tag{2.15}$$

meaning that the current density decreases by a factor of e in the liquid metal with every 4 millimeters of depth.

2.6 Current Density

Current density is the measure of the amount of current passing through a cross-sectional area. To determine the cross-sectional area with which the current flows we must first define

the path by which it is able to travel through the liquid metal. We have constrained the current path to the z direction. We are ignoring the aspects of the current that may flow in a direction other than this, such as down and radially at the same time. This constraint limits the flow of current to the cylindrical cross section in Figure 2.8.

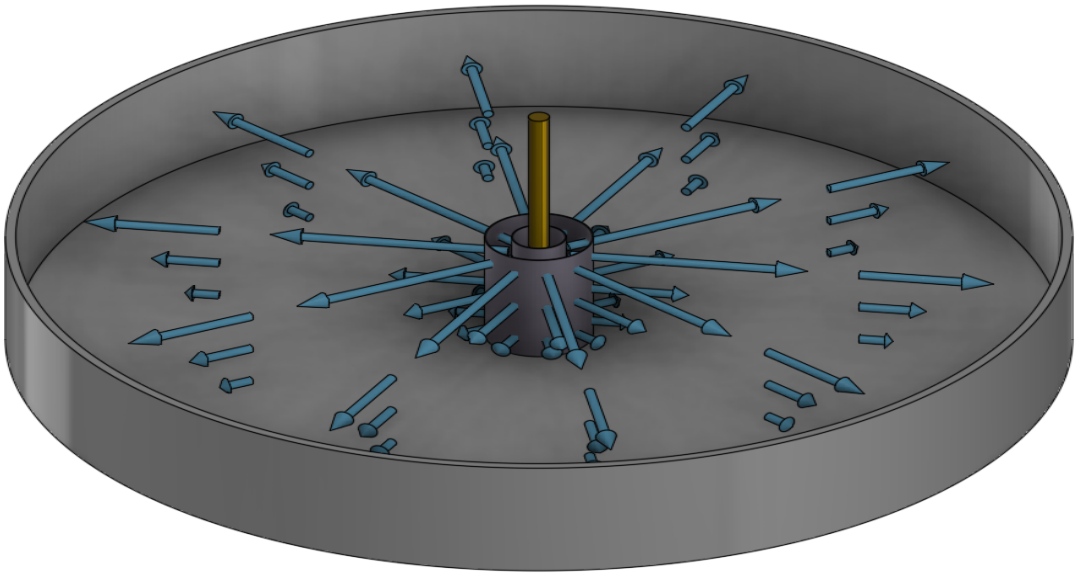

Figure 2.7: Isometric depiction of the current density geometry. The current density is greatest near the surface of the liquid metal. The current density decreases with depth due to the skin depth.

The system is axisymmetric so that in cylindrical coordinates the strength of the current density can be found in the r-z plane. The current density is thus calculated as the relative strength of the current at depth z over the cross-sectional area at a given radius inside of the liquid metal. Equation 2.16 calculates the current density of the liquid metal.

$$\mathbf{j}(r,z) = \frac{I_0 e^{-z/d}}{2\pi r h}\hat{r} \quad \left[\frac{\mathrm{A}}{\mathrm{m}^2}\right] \tag{2.16}$$

Figure 2.9 and Figure 2.10 show the current density within the liquid metal. The wire is located at the origin in the upper-left corner. The values of current density are logarithmic.

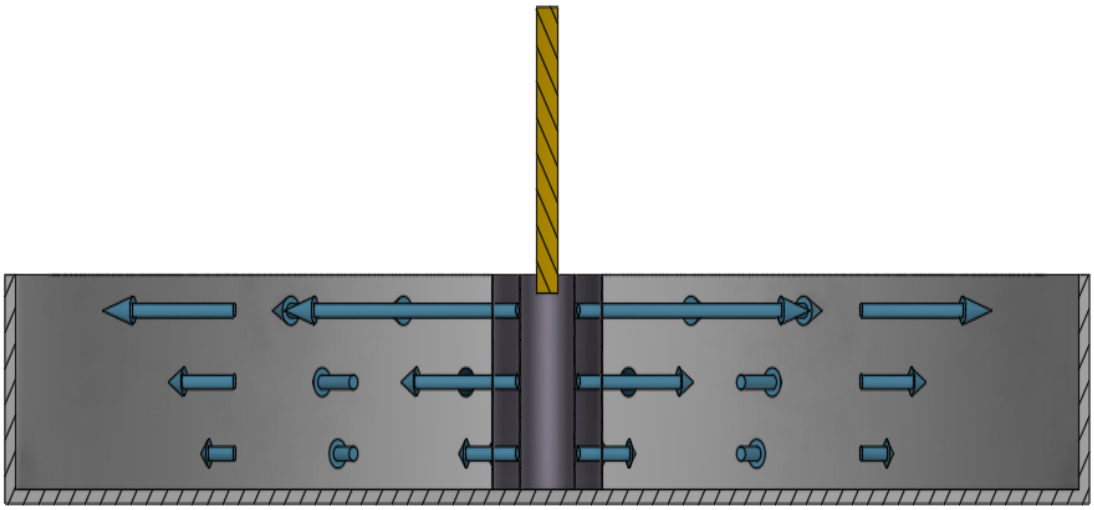

Figure 2.8: Cross-section depiction of the current density geometry. The current density is greatest near the surface of the liquid metal. The current density decreases with depth due to the skin depth.

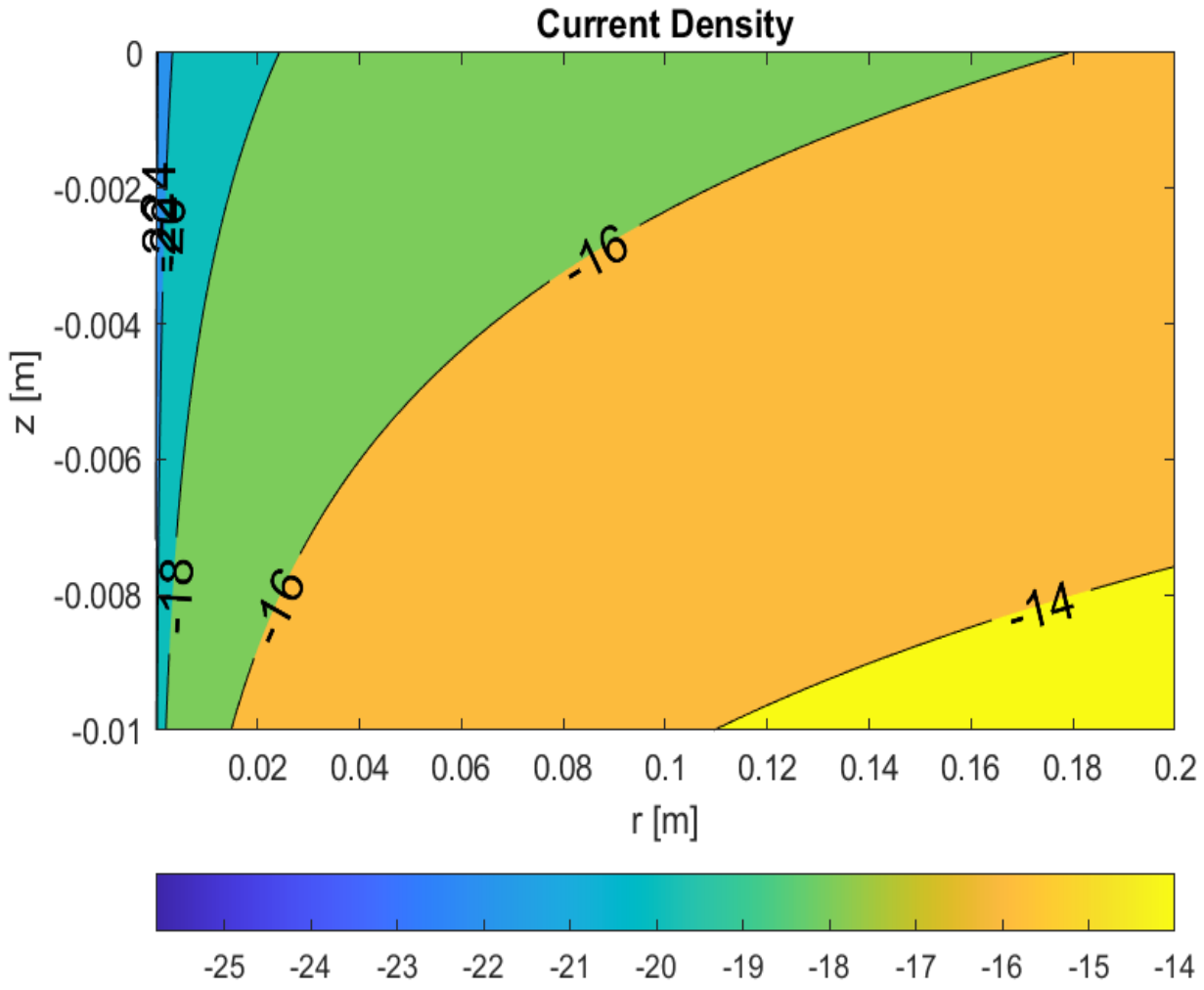

Figure 2.9: Contour plot of the current density in the r-z plane. Current density units are $log_{10}([\text{A m}^{-2}])$. The wire is located at the origin in the upper-left corner. The magnitude of the current density decreases with distance from the origin. This figure shows the calculated current density for depth 1 cm and radius 20 cm.

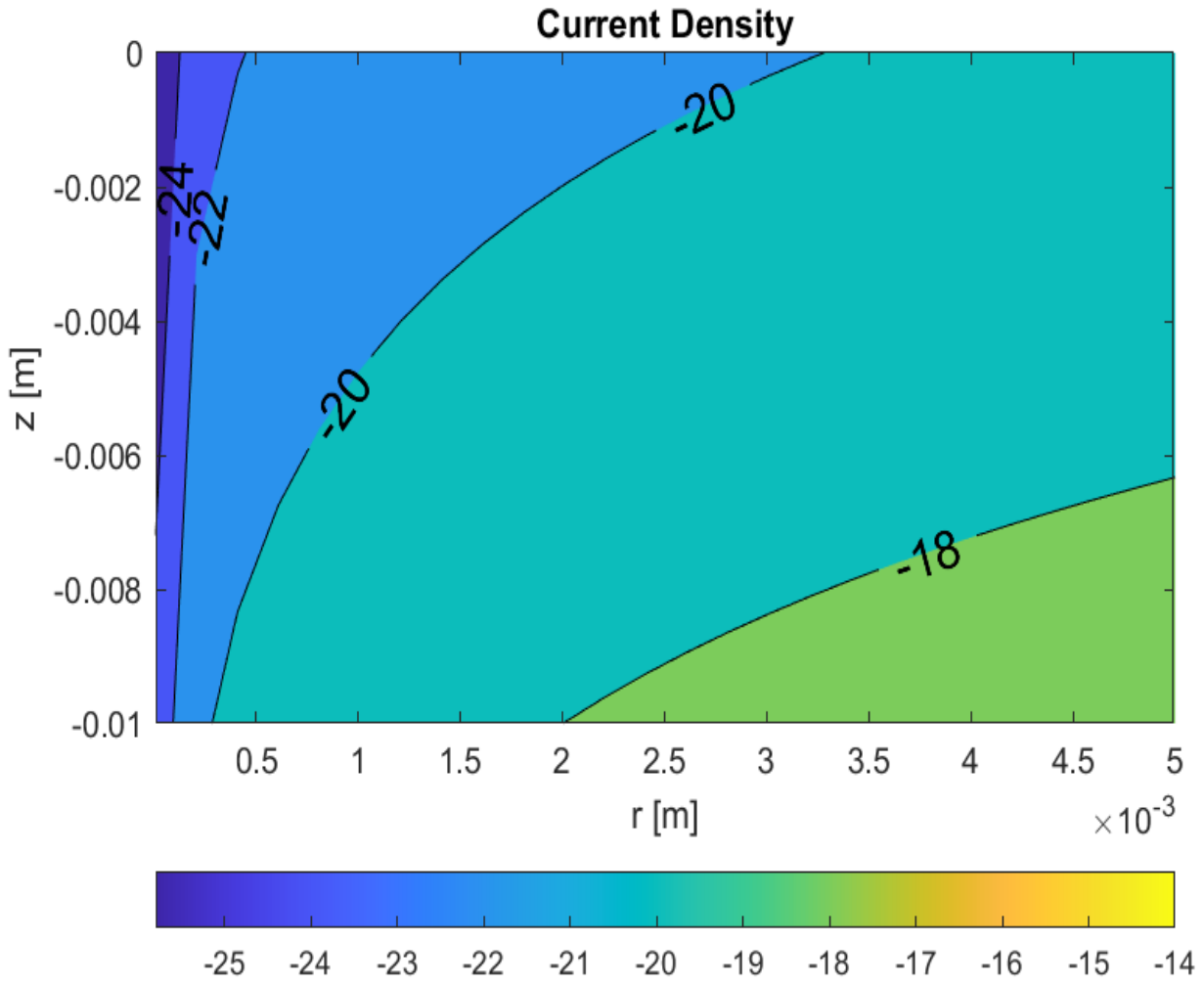

Figure 2.10: Contour plot of the current density in the r-z plane. Current density units are $log_{10}([\text{A m}^{-2}])$. The wire is located at the origin in the upper-left corner. The magnitude of the current density decreases with distance from the origin. This figure shows the calculated current density for depth 1 cm and radius 1 cm.

2.7 Pressure Gradient

The pressure gradient in the current density method is the cross product of the magnetic field, B, and the current density, $\mathbf{j}$, found in Equations 2.5 and 2.16, respectively. The pressure gradient acts in the -z direction due to the cross between the radial, r, components of the current density and azimuthal, θ, components of the magnetic field. Pressure gradient has units Nm^{-3}.

$$\nabla P = \mathbf{j} \times \mathbf{B} \tag{2.17}$$

$$\nabla P = \begin{array}{ll} -\left(\frac{\mu_0 I_0^2}{4\pi^2 R_{wire}^2 h}\right) \hat{z} \left[\frac{\mathrm{N}}{\mathrm{m}^3}\right], & r < R_{wire} \\ -\frac{\mu_0 I_0^2}{2\pi^2 r h} \hat{z} \left[\frac{\mathrm{N}}{\mathrm{m}^3}\right], & r > R_{wire} \end{array} \tag{2.18}$$

Plots of the pressure gradient are shown in Figure 2.12. The pressure gradient behaves similarly to the current density. The magnitude of the pressure gradient decreases with distance from the origin. The wire is located at the origin in the upper-left corner. The values of pressure gradient are logarithmic. The magnitude of the pressure gradient is greatest along at $r = 0$ m and lowest in the bottom right corner. The rate at which the magnitude of the pressure gradient diminishes is proportional to $1/r^2$ instead of $1/r$ in the current density.

Equation 2.19 finds the pressure in created by the current density method.

$$P = \nabla P \cdot d \left[\frac{\mathrm{N}}{\mathrm{m}^2}\right] \tag{2.19}$$

In Equation 2.19, P is the pressure, ∇P is the pressure gradient, and $d = 4.0 \times 10^{-3}$ m is the skin depth, as found in Equation 2.15 and the depth over which the pressure is averaged.

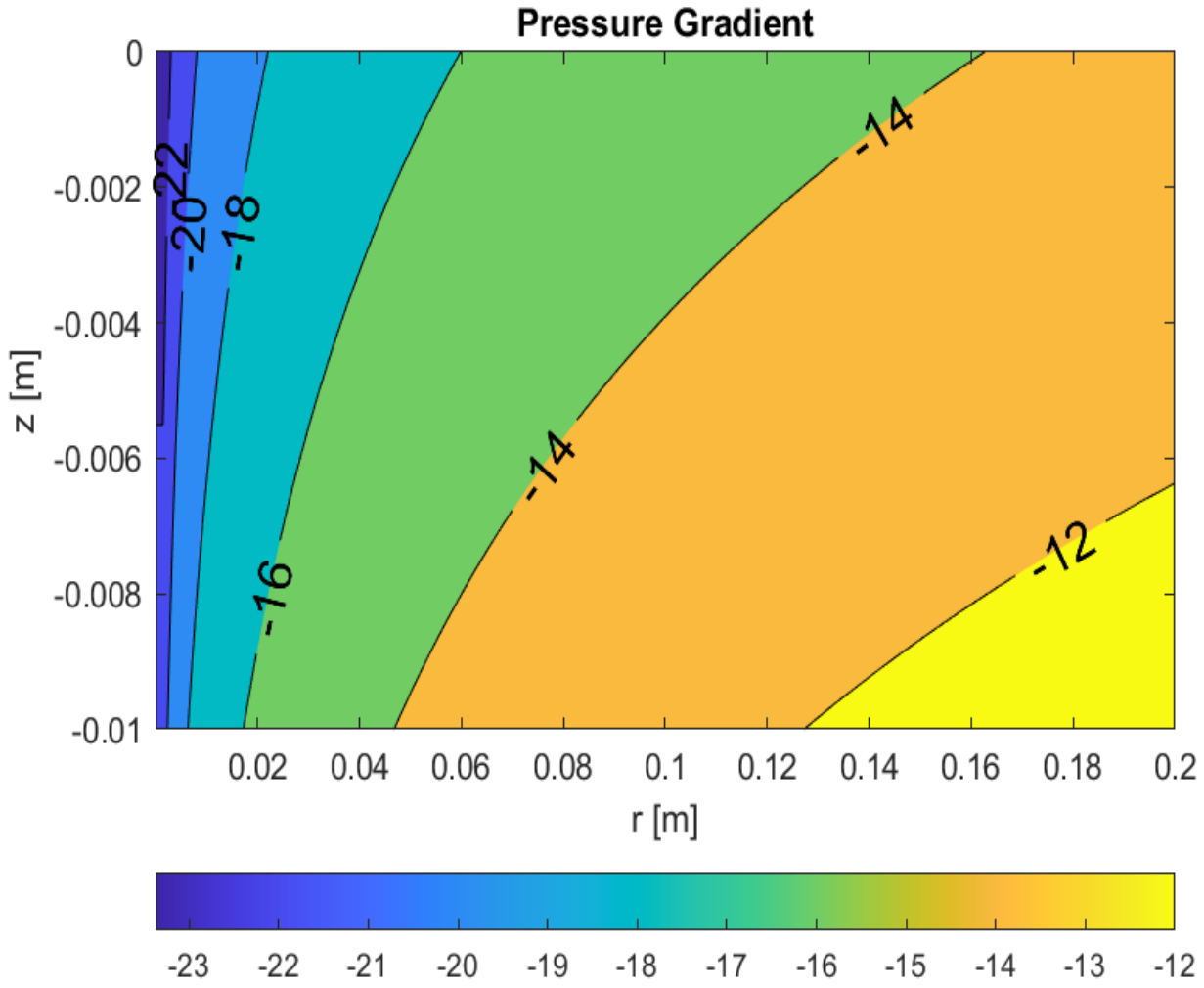

Figure 2.11: Contour plot of the pressure gradient in the r-z plane. The units for the pressure gradient are $log_{10}([\text{N m}^{-3}])$. The wire is located at the origin in the upper-left corner. The magnitude of the pressure gradient decreases with distance from the origin. This figure shows the calculated pressure gradient for depth 1 cm and radius 20 cm.

The peak pressure is $P_{CD} = -3.6 \times 10^7$ Nm^{-2}. Figure 2.12 shows the pressure generated by the current density. The current density plot shows that this model predicts the pressure to be constant within the radius of the wire, $r_{wire} = 1.5 \times 10^{-3}$ m.

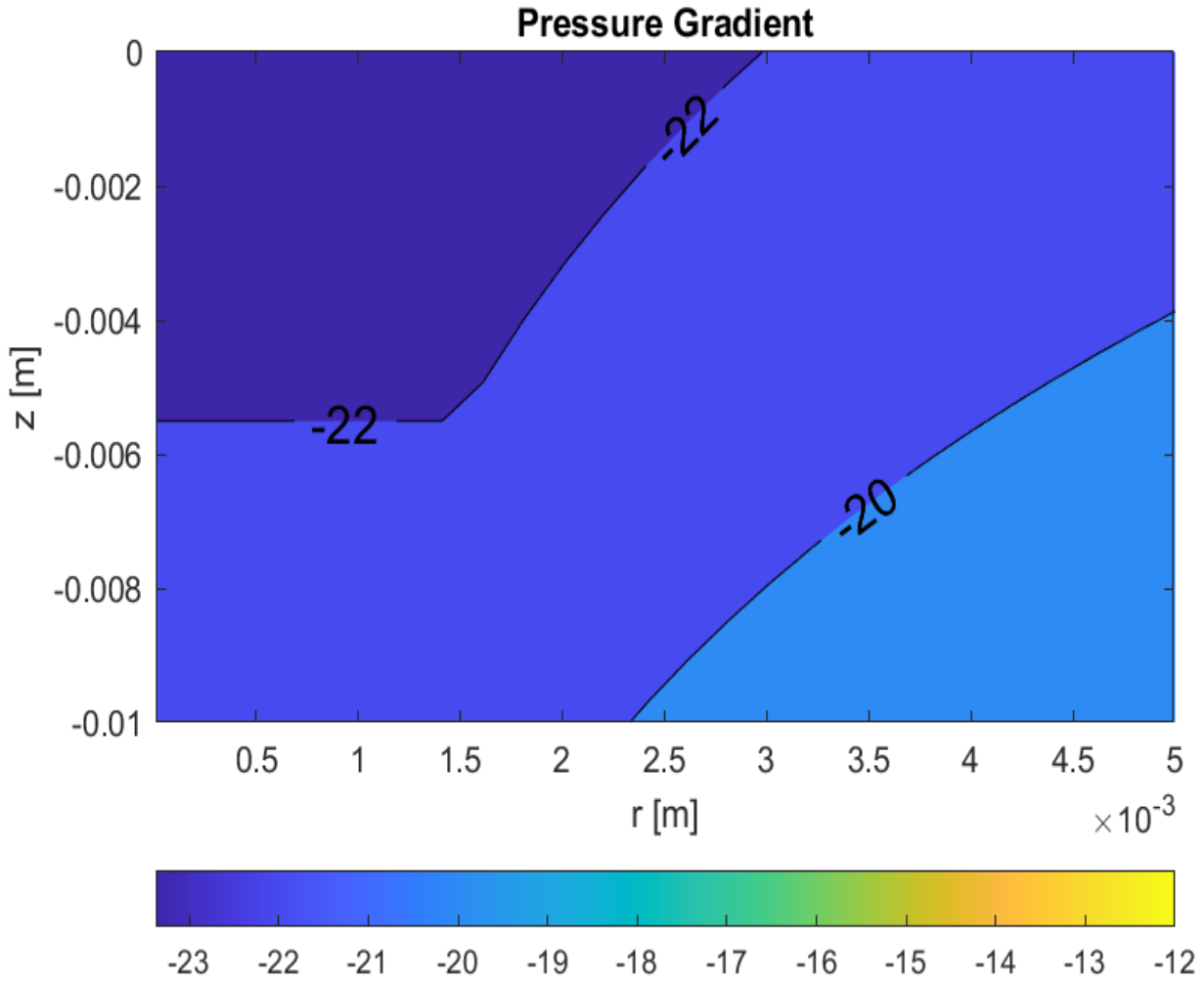

Figure 2.12: Contour plot of the pressure gradient in the r-z plane. The units for the pressure gradient are $log_{10}([\text{N m}^{-3}])$. The wire is located at the origin in the upper-left corner. The magnitude of the pressure gradient decreases with distance from the origin. This figure shows the calculated pressure gradient for depth 1 cm and radius 21 cm.

2.8 Magnetic Pressure

Figure 2.14 shows the magnetic pressure calculated using Equation 2.11. The peak magnetic pressure is $P_{mag} = -6.3 \times 10^7$ Nm^{-2}. The magnitude of the magnetic pressure is higher than

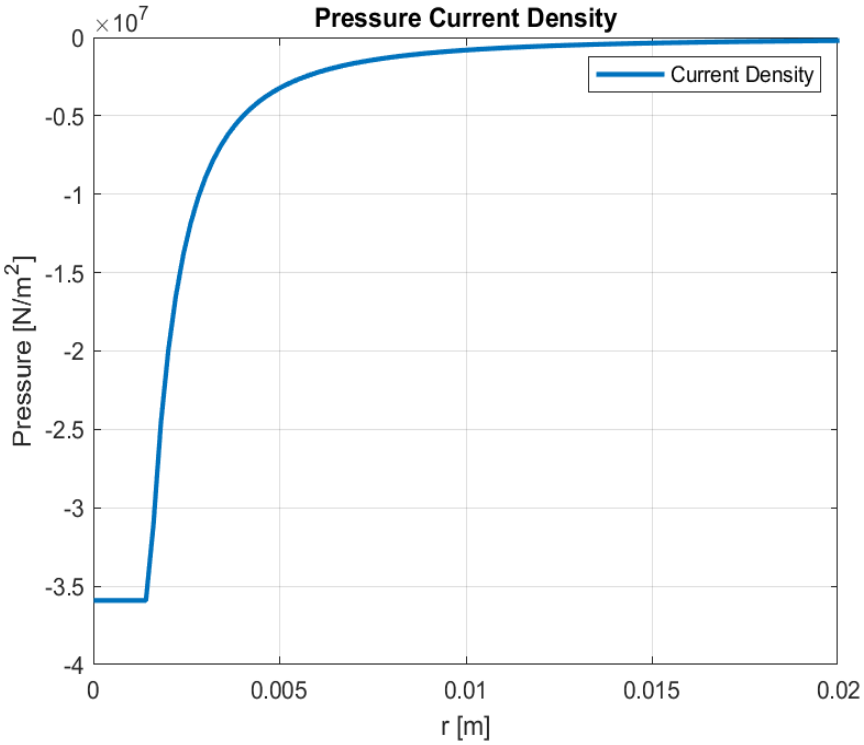

Figure 2.13: Pressure calculated from the current density. The pressure from the current density is constant within the radius of the wire. The pressure decreases rapidly outside of the radius of the wire.

that of the pressure calculated from the current density and occurs over a narrower range. The pressure used in calculating the initial displacement is found by averaging the pressure over a range in the r direction. In Section 4.5, the range over which the pressure is averaged is varied and the two methods are directly compared.

Table 2.2: Peak pressures for magnetic pressure and current density pressure

Method	Pressure Peak [N/m^2]	Averaging Range [mm]	Average Pressure [N/m^2]
Magnetic Pressure	-6.3×10^7	2.5	1.197×10^8
Current Density	-3.6×10^7	2.5	1.21×10^8

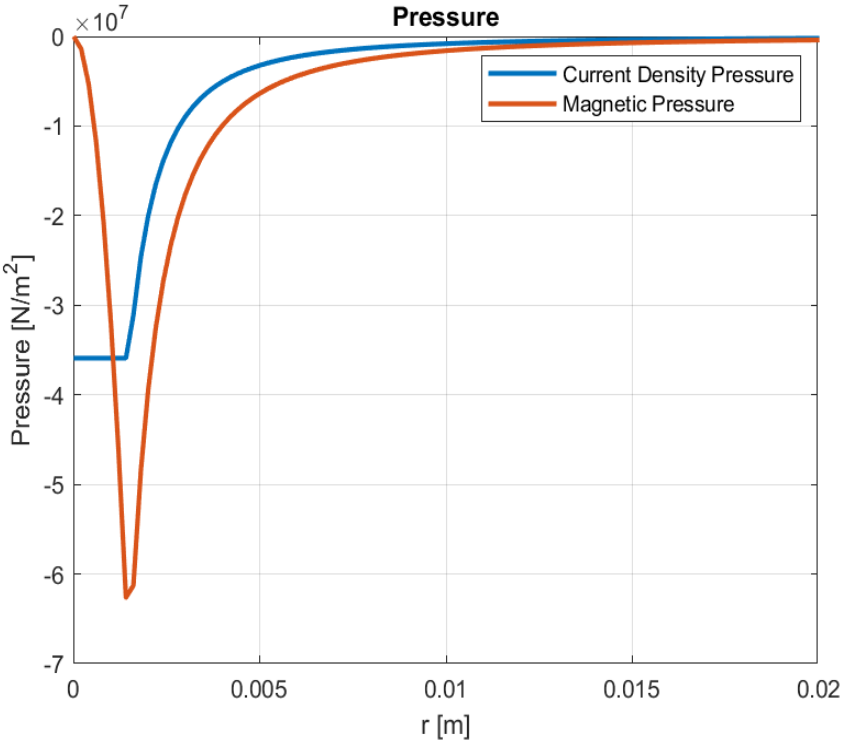

Figure 2.14: Magnetic pressure and current density pressure plot. The magnetic pressure has a larger magnitude than the current density pressure. The magnetic pressure increases in magnitude from the origin to the radius of the wire.

2.9 Free Surface Displacement

A kinematic approach was taken to determine how the pressure changes the surface elevation. The kinematic approach uses the pressure approximations from Figure 2.14. Pressure applied to the surface of the liquid metal displaces a mass of the liquid metal, m_a. The mass accelerates over the same time interval as the initial current pulse is active.

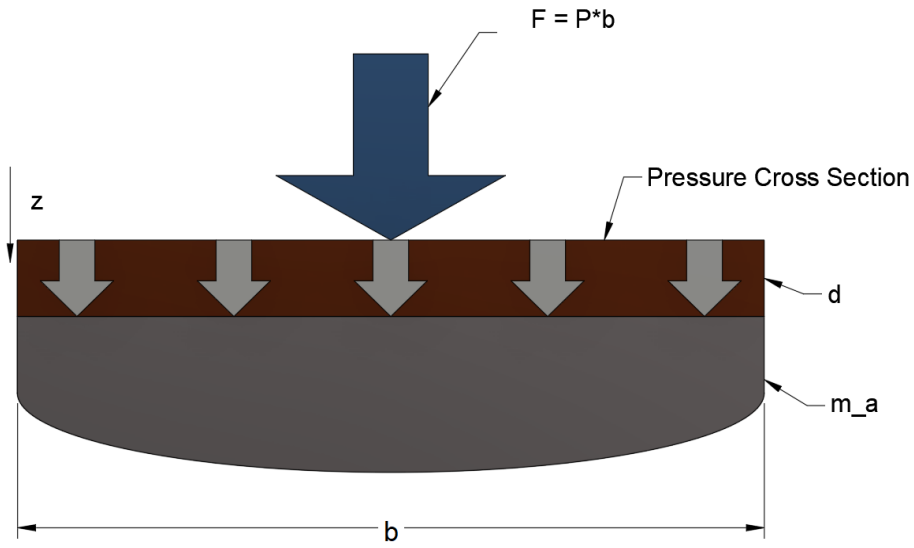

Figure 2.15: Free body diagram for the acceleration of mass due to the exerted force, F_{ext}. The pressure is applied across the b range in the z-direction.

The force exerted, F_{ext}, is equal to the pressure times the surface area to which the pressure is applied. The surface area is a circle of diameter b. The skin depth, d, is the depth range over which the pressure was averaged in the current density approach. Due to the rapid decrease in strength of the pressure outside of the radius of the wire the range has been constrained to under 1 cm. We can think of the force exerted by the pressure as a plate impacting and accelerating the liquid metal.

$$m_a = \rho\pi\frac{b^2}{8} \tag{2.20}$$

The next step in finding the change in displacement is to perform simplified kinematic integration of the pressure. The pressure is constant over the surface area and the time interval of the pulse, 0.5 μs. Equation 2.22 finds the initial free surface displacement during this time.

$$F_{ext} = m_a \ddot{z} \tag{2.21}$$

$$\begin{aligned} Z(t = t_0) &= \int \int \left[\frac{F_{ext}}{m_a} \right] dt^2 \\ &= \frac{F_{ext}}{m_a} \left(\frac{t_0^2}{2} \right) \end{aligned} \tag{2.22}$$

In Equation 2.22 Z is the final displacement of the accelerated mass at t_0. t_0 is the time duration of the current pulse. Equation 2.22 uses only inertia to determine the displacement. Hydrodynamic effects are ignored when finding the displacement of the liquid metal.

Table 2.3 provides the values held constant in the initial calculation of the liquid metal free surface.

Table 2.3: Displacement Constants

I_0 [kA]	t_o [μs]	ω [kHz]	Tin %	Skin Depth [mm]	b Range
100	50	20	50	4	2.5

Table 2.4 provides the displacement values for the magnetic pressure and current density methods. The magnetic pressure is found using Equation 2.11 and the pressure in the current density method is found using Equation 2.19. The difference in pressure between the two methods is 0.4 MPa. Equation 2.22 provides the initial surface displacement for both methods. The difference in initial surface displacement between the two methods is 0.44 mm.

Table 2.4: Displacement Values

Magnetic Pressure [MPa]	Current Density Pressure [MPa]	Difference [MPa]
-29.9	-30.3	0.4
Magnetic Pressure Displacement [mm]	Current Density Displacement [mm]	Difference [mm]
-2.23	-2.67	0.44

Chapter 3

Fluid Formulation

This chapter introduces the fluid components of the analytical solution. The fluid components of the analytical solution are found solving the Cauchy-Poisson wave equations with appropriate initial conditions for the system. The solutions for the Cauchy-Poisson wave equation solve for the surface elevation, η, and the velocity potential, ϕ. The surface elevation describes how the waveform created by the initial conditions changes with time. The velocity potential is a scalar potential used to describe the time dependent potential flow associated with the wave propagation.

This chapter solves the axisymmetric Cauchy-Poisson problem. In later sections, the analytical solution, simulated using MATLAB, is compared with the high-fidelity computational fluid dynamics solver, StarCCM+, for validation. This system involves inviscid incompressible liquid of finite depth with a free surface. In this analytical solution inviscid and incompressible means that the shear stresses and vorticity induced by viscosity and compressibility of the fluid are ignored. Hence, the liquid has constant density, ρ, and additionally negligible surface tension.

3.1 Axisymmetric Cauchy-Poisson Water

The axisymmetric Cauchy-Poisson system is solved in cylindrical coordinates, (r, θ, z). The system of equations and corresponding boundary conditions are presented below.

$$\nabla^2\phi = \phi_{rr} + \frac{1}{r}\phi_r + \phi_{zz} = 0, \quad -h < z \leq 0, \quad \infty < r < \infty, \quad t > 0 \tag{3.1}$$

$$\left.\begin{aligned} \phi_z - \eta_t &= 0 \\ \phi_t + g\eta &= 0 \end{aligned}\right\} \quad \text{on } z = 0, \quad t > 0 \tag{3.2}$$

$$\phi_z = 0 \quad \text{on } z = -h, \quad t > 0 \tag{3.3}$$

Equation 3.1 describes how the free surface motion is governed by the velocity potential, $\phi(r, z, t)$. Equation 3.1 details how the components which describe the motion (r, θ, z) are connected: an increase in one direction results in a decrease in another. Equations 3.2 describe the linearized kinetic and dynamic free surface boundary conditions. Equation 3.3 is the final boundary condition, which is impermeable boundary condition where the vertical velocity, ϕ_z, is zero. The initial conditions in Equation 3.4 and 3.5 state that the velocity potential is zero and the surface elevation is non-zero. This is the first major simplification of the fluid formulations. This simplification limits the solution to only after the time of maximum surface elevation displacement.

$$\phi(r, 0, 0) = 0 \tag{3.4}$$

$$\eta(r, 0) = \eta_0(r) \tag{3.5}$$

3.2 Transforms

The goal of this section is to find solutions for the surface elevation, and to a lesser extent, the velocity potential. The system of boundary and initial conditions are not solvable in their current form. To solve the system of equations analytically they are transformed, using a combination of Laplace and Hankel transforms. The Laplace transform converts the real time variable, t, to the complex variable, s. The Hankel transform is similar to the Fourier transform except in that it converts the real spatial variable, r, to the complex variable, k. We leave the z coordinate system as is. Equation 3.6 is a representation of the combined transform we used in finding the transformed velocity potential.

$$\widetilde{\overline{\phi}}(k,z,s) = \int_0^\infty e^{-st}dt \int_0^\infty rJ_0(kr)\phi(r,z,t)dr \tag{3.6}$$

The following are the transformations of the initial velocity potential Equation 3.4.

$$\begin{aligned} L\{H\{\phi(r,0,0) = 0\}\} \\ \widetilde{\overline{\phi}}(k,0,0) = 0 \end{aligned} \tag{3.7}$$

Then the initial surface elevation is given by Equation 3.5.

$$\begin{aligned} L\{H\{\eta(r,0) = \eta_0(r)\}\} \\ L\{\widetilde{\eta}(k,0) = \widetilde{\eta_0}(k)\}\} \\ \widetilde{\overline{\eta}}(k,0) = \widetilde{\eta_0}(k) \end{aligned} \tag{3.8}$$

The following is the transformation of the first boundary condition in Equation 3.1.

$$\begin{aligned} L\{H\{\nabla^2\phi = \phi_{rr} + \frac{1}{r}\phi_r + \phi_{zz} = 0\}\} \\ L\{-k^2\widetilde{\phi} + \widetilde{\phi}_{zz} = 0\} \\ -k^2\widetilde{\overline{\phi}} + \widetilde{\overline{\phi}}_{zz} = 0 \\ \left(\frac{d^2}{dz^2} - k^2\right)\widetilde{\overline{\phi}} = 0 \end{aligned} \tag{3.9}$$

Next is the transformation for the second boundary condition in Equation 3.2.

$$\begin{aligned} H\{L\{\phi_z - \eta_t = 0\}\} \\ H\{\frac{d\overline{\phi}}{dz} - (s\,\overline{\eta}(r,s) - \overline{\eta}(r,0)) = 0\} \\ H\{\frac{d\overline{\phi}}{dz} - s\,\overline{\eta}(r,s) = -\eta_0(r)\} \\ \frac{d\widetilde{\overline{\phi}}}{dz} - s\,\widetilde{\overline{\eta}}(k,s) = -\widetilde{\eta_0}(k) \end{aligned} \tag{3.10}$$

Next is the transformation for the third boundary condition in Equation 3.2.

$$\begin{aligned} H\{L\{\phi_t + g\eta = 0\}\} \\ H\{s\overline{\phi} - \overline{\phi}(r,z,0) + g\,\overline{\eta}(r,s) = 0\} \end{aligned} \tag{3.11}$$

The free surface boundary condition is imposed at $z = 0$ thus $\phi(r,z,0) = \phi_0 = 0$.

$$\begin{aligned} H\{s\,\overline{\phi} + g\,\overline{\eta} = 0\} \\ s\,\widetilde{\overline{\phi}} + g\,\widetilde{\overline{\eta}} = 0 \end{aligned} \tag{3.12}$$

Last is the transformation for the fourth boundary condition in Equation 3.3

$$\begin{aligned} H\{L\{\phi_z = 0\}\} \\ \widetilde{\overline{\phi}}_z = 0 \end{aligned} \tag{3.13}$$

The transformed boundary conditions and initial conditions are as follows. Note that the domains in which the boundary conditions are valid are also transformed.

$$\left(\frac{d^2}{dz^2} - k^2\right)\widetilde{\overline{\phi}} = 0, \quad 0 \le r < \infty \quad -h \le z < 0, \quad s > 0 \tag{3.14}$$

$$\left.\begin{aligned} \widetilde{\overline{\phi}} - s\,\widetilde{\overline{\eta}} = -\widetilde{\eta}_0(k) \\ s\,\widetilde{\overline{\phi}} + g\,\widetilde{\overline{\eta}} = 0 \end{aligned}\right\} \text{on } z = 0, \quad s > 0 \tag{3.15}$$

$$\widetilde{\overline{\phi}} = 0, \quad z = -h \tag{3.16}$$

The transformed initial conditions are

$$\widetilde{\overline{\phi}}(k, 0, 0) = 0 \tag{3.17}$$

$$\widetilde{\overline{\eta}}(k, 0) = \widetilde{\eta}_0(k). \tag{3.18}$$

3.3 General Form Solutions

The general solution used here is based upon solutions from Lokenath Debnath 1990 [2]. The general solution for the velocity potential is

$$\widetilde{\overline{\phi}}(k, z, s) = \overline{A}\,\frac{\cosh\left(k(z+h)\right)}{\cosh\left(k\ h\right)}. \tag{3.19}$$

The coefficient $\overline{A}$ must be solved to find the solution for $\widetilde{\overline{\phi}}$. Solving boundary condition 3 for $\widetilde{\overline{\eta}}$ gives

$$s\,\widetilde{\overline{\phi}} + g\,\widetilde{\overline{\eta}} = 0 \tag{3.15}$$

$$\widetilde{\overline{\eta}} = -\frac{s}{g}\widetilde{\overline{\phi}}. \tag{3.20}$$

Next the isolated $\widetilde{\overline{\eta}}$ term in equation 3.20 is substituted into the second boundary condition, Equation 3.15. This produces an equation that is dependent on an initial condition for surface elevation, the function we wish to solve for, and its derivative with respect to z.

$$\widetilde{\overline{\phi}}_z - s\,\widetilde{\overline{\eta}} = -\widetilde{\eta}_0(k) \tag{3.15}$$

$$\widetilde{\overline{\phi}}_z - s\left(-\frac{s}{g}\widetilde{\overline{\phi}}\right) = -\widetilde{\eta}_0(k)$$

$$\widetilde{\overline{\phi}}_z + \frac{s^2}{g}\widetilde{\overline{\phi}} = -\widetilde{\overline{\eta}}_0(k) \tag{3.21}$$

To solve Equation 3.21, we take the z derivative of $\widetilde{\overline{\phi}}$, $\widetilde{\overline{\phi}}_z$. The fourth boundary condition, Equation 3.3, dictates that the derivative is taken at $z = 0$.

$$\widetilde{\overline{\phi}}|_{z=0} = \overline{A}\,\frac{\cosh\left(k(z+h)\right)}{\cosh kh} \tag{3.19}$$

$$\widetilde{\overline{\phi}}|_{z=0} = \overline{A} \tag{3.22}$$

$$\widetilde{\overline{\phi}}_z|_{z=0} = \overline{A}k\frac{\sinh\left(k(z+h)\right)}{\cosh\left(kh\right)}|_{z=0} \tag{3.23}$$

$$\widetilde{\overline{\phi}}_z|_{z=0} = \overline{A}\,k\tanh kh \tag{3.24}$$

When the general solution is at $z = 0$, the solution becomes equal to $\overline{A}$. The derivative, ϕ_z,

at $z = 0$ is Equation 3.24. Plugging these results into Equation 3.21 gives $\overline{A}$.

$$\widetilde{\overline{\phi}}_z + \frac{s^2}{g}\widetilde{\overline{\phi}} = -\widetilde{\overline{\eta}}_0(k) \tag{3.21}$$

$$\begin{aligned} \overline{A}\, k \tanh(kh) + \frac{s^2}{g}\overline{A} &= -\widetilde{\eta}_0(k) \\ \overline{A}(g\, k \tanh(kh) + s^2) &= -g\, \widetilde{\eta}_0(k) \end{aligned} \tag{3.25}$$

$$\overline{A} = -\frac{g\, \widetilde{\eta}_0(k)}{\alpha^2 + s^2} \tag{3.26}$$

$$\alpha^2 = g\, k \tanh(kh) \tag{3.27}$$

In Equation 3.27, α^2 is the wave frequency. The wave frequency is a measure of how fast waves travel in a medium. Using the solved value of $\overline{A}$ the general solution for ϕ is known. To solve for η, we first take the previously found Equation 3.15 at z and substitute in $\phi|_z = 0$ into it.

$$\widetilde{\overline{\eta}} = -\frac{s}{g}\widetilde{\overline{\phi}}|_{z=0} \tag{3.28}$$

$$= -\frac{s}{g}\left(-\frac{g\, \widetilde{\eta}_0(k)}{\alpha^2 + s^2}\right)\frac{\cosh(k(z+h))}{\cosh(k\, h)}|_{z=0}$$

$$\widetilde{\overline{\eta}} = \frac{s\, \widetilde{\eta}_0(k)}{\alpha^2 + s^2} \tag{3.29}$$

Equation 3.30 contains the transformed values for the velocity potential and the surface elevation. Both terms are dependent on the initial surface elevation, the wave frequency, the wave number, k, and the frequency, s.

$$\left[\widetilde{\overline{\phi}}(k,z,s), \widetilde{\overline{\eta}}(k,s)\right] = \left[-\frac{g\, \widetilde{\eta}_0(k)}{(s^2+\alpha^2)}\frac{\cosh(k(z+h))}{(k\, h)}, \frac{s\, \widetilde{\eta}_0(k)}{(s^2+\alpha^2)}\right] \tag{3.30}$$

The next step in the process of solving the transformed solutions involves the inverse transforms. The inverse Laplace and Fourier transforms are now applied to Equation 3.30. In

Equation 3.32 $J_0(kr)$ is the Bessel function of the first kind of order zero.

$$\widetilde{\overline{\phi}}(k,z,s) = \int_0^\infty e^{-st}dt \int_0^\infty rJ_0(kr)\left(\frac{-g\ \widetilde{\eta}_0(k)}{(s^2+\alpha^2)}\frac{\cosh\left(k(z+h)\right)}{\cosh\left(k\ h\right)}\right)dr \tag{3.31}$$

Equation 3.32 is the inverse transform of the velocity potential.

$$\phi(r,z,t) = -g\int_0^\infty kJ_0(kr)\widetilde{\eta}_0(k)\left(\frac{\sin\left(\alpha t\right)}{\alpha}\right)\frac{\cosh\left(k(z+h)\right)}{\cosh\left(k\ h\right)}dk \tag{3.32}$$

Equation 3.33 is the inverse transform of the surface elevation and includes the same Bessel function.

$$\widetilde{\overline{\eta}}(k,s) = \int_0^\infty e^{-st}dt \int_0^\infty rJ_0(kr)\left(\frac{-g\ \widetilde{\eta}_0(k)}{(s^2+\alpha^2)}\right)dr \tag{3.33}$$

$$\eta(r,t) = \int_0^\infty kJ_0(kr)\overline{\eta}_0(k)\cos\left(\omega\ t\right)dk \tag{3.34}$$

Both solutions retain their dependence on the appropriate variables. These solutions are still not analytically solvable. Approximations must be made to Equation 3.34 to analytically on for the surface displacement.

3.4 Asymptotic Approximation Using Stationary of Phase Method

The stationary of phase method is valid when the wave number, k, is asymptotically small. Evaluating asymptotic form for $kr \to \infty$ result in Equation 3.36 gives

$$J_0(kr) \approx \left(\frac{2}{\pi k\ r}\right)^{1/2}\cos\left(k\ r - \frac{\pi}{4}\right). \tag{3.35}$$

Using Equation 3.35, the inverse transformed surface elevation in Equation 3.34 becomes

$$\begin{aligned}\eta(r,t) &\approx \left(\frac{2}{\pi r}\right)^{1/2} \int_0^\infty \sqrt{k}\ \overline{\eta_0}(k) \cos\left(k\ r - \frac{\pi}{4}\right) \cos\left(\omega\ t\right) dk \\ &= (2\pi r)^{-1/2} Re \int_0^\infty \sqrt{k}\ \overline{\eta_0}(k) \exp\left[i\left(\omega\ t - k\ r + \frac{\pi}{4}\right)\right] dk.\end{aligned} \tag{3.36}$$

The stationary phase method must take a stationary point into account. Here the stationary point is $k_1 = \frac{gt^2}{4r^2}$ which is the root of $\alpha'(k) = r/t$. The term k_1 is of special significance as it is a time evolving variable that impacts the surface elevation.

The limit of the stationary phase is that $gt^2 >> 4r$. Here, much greater than is defined as an order of magnitude and is taken into direct account in the simulation section. The surface elevation formula that is used in the simulation is given as Equation 3.37

$$\eta(r,t) \approx \left[\frac{k_1}{r\ t|\omega''(k_1)|}\right]^{1/2} \overline{\eta_0}(k_1) \cos\left[t\ \omega(k_1) - k_1\ r\right]. \tag{3.37}$$

The last step before the computation of the surface elevation equation is to find an equation for the initial surface elevation and its transform. The form of this equation is a guess as to how the free surface is displaced after the pulse is applied to it. The equation form used is Equation 3.38.

$$\eta_0(r,0) = -Ze^{-r^2/c^2} \tag{3.38}$$

The transform of the initial surface elevation equation is

$$\overline{\eta_0}(k,0) = -Z\left(\frac{c^2}{2}\right) e^{(-k^2c^2/4)}, \tag{3.39}$$

where Z is the initial surface displacement given in Equation 2.22. The untransformed Equation 3.38 is plotted in Figure 3.1.

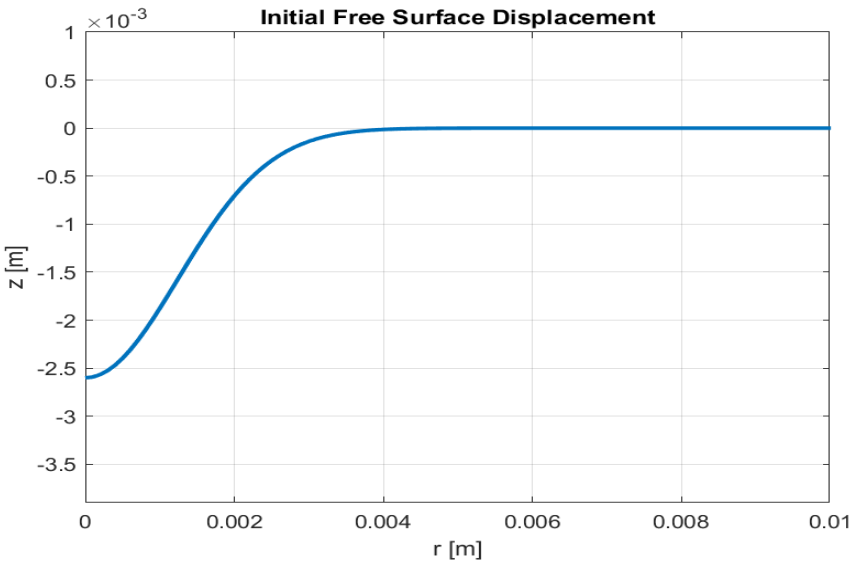

Figure 3.1: Plot of the initial free surface displacement.

Chapter 4

Analytical Solution

The goal of this chapter is to investigate how Equation 3.37 and Equation 3.39 describe the free surface elevation over time. Equation 3.39 directly describes how the electromagnetic and kinematic equations impact the initial free surface displacement. Equation 3.37 directly describes the free surface displacement over time. These equations are meant to inform further projects. This chapter investigates the impact of variables such as, material type, current strength, current pulse length, depth of liquid metal on the initial free surface displacement of the liquid metal and the subsequent waveform. Changing these variables can affect the free surface displacement. The current strength, and current pulse length are related to plasma and fusion generation in Z-pinches. The depth and material properties of the liquid metal are chosen to investigate for insight into additional experiments and new devices. Variables such as the range over which the pressure is applied, b range, are investigated because they have not been empirically determined. The analysis of these variables and their ranges may be useful for informing the construction of new devices.

4.1 Analytical Solution Results

Equation 3.37 is plotted over time in Figure 4.1 using the initial free surface displacement of both the magnetic pressure and current density methods. Table 2.4 shows the difference between the initial displacements of the two methods. The difference between the two initial

displacements is 0.44 mm. Figure 4.1 shows the differences between the two methods over time. Other than the amplitude, the waveform behaves identically. The amplitude is greatest and most negative in the beginning, then it begins to oscillate. Over time, the amplitude decreases, and the waveform broadens, due to the dispersion term given by Equation 3.27. Table 4.1 shows the constants used in the baseline analytical solution in Figure 4.1.

Table 4.1: Analytical Solution Constants

I_0 [kA]	t_0 [μ s]	ω [kHz]	Tin %	Skin Depth [mm]	b Range [mm]	Depth [mm]
100	50	20	50	4	2.5	10

Taking these two approaches as the extreme possibilities for the displacement, the current density approach returns the larger magnitude of displacement. The difference between the results is due to the current density's dependence on additional variables over the magnetic pressure approach. The current density approach depends on the material constants of the liquid metal, and therefore the skin depth. The magnetic pressure approach depends only on the current in the wire and the resulting magnetic field.

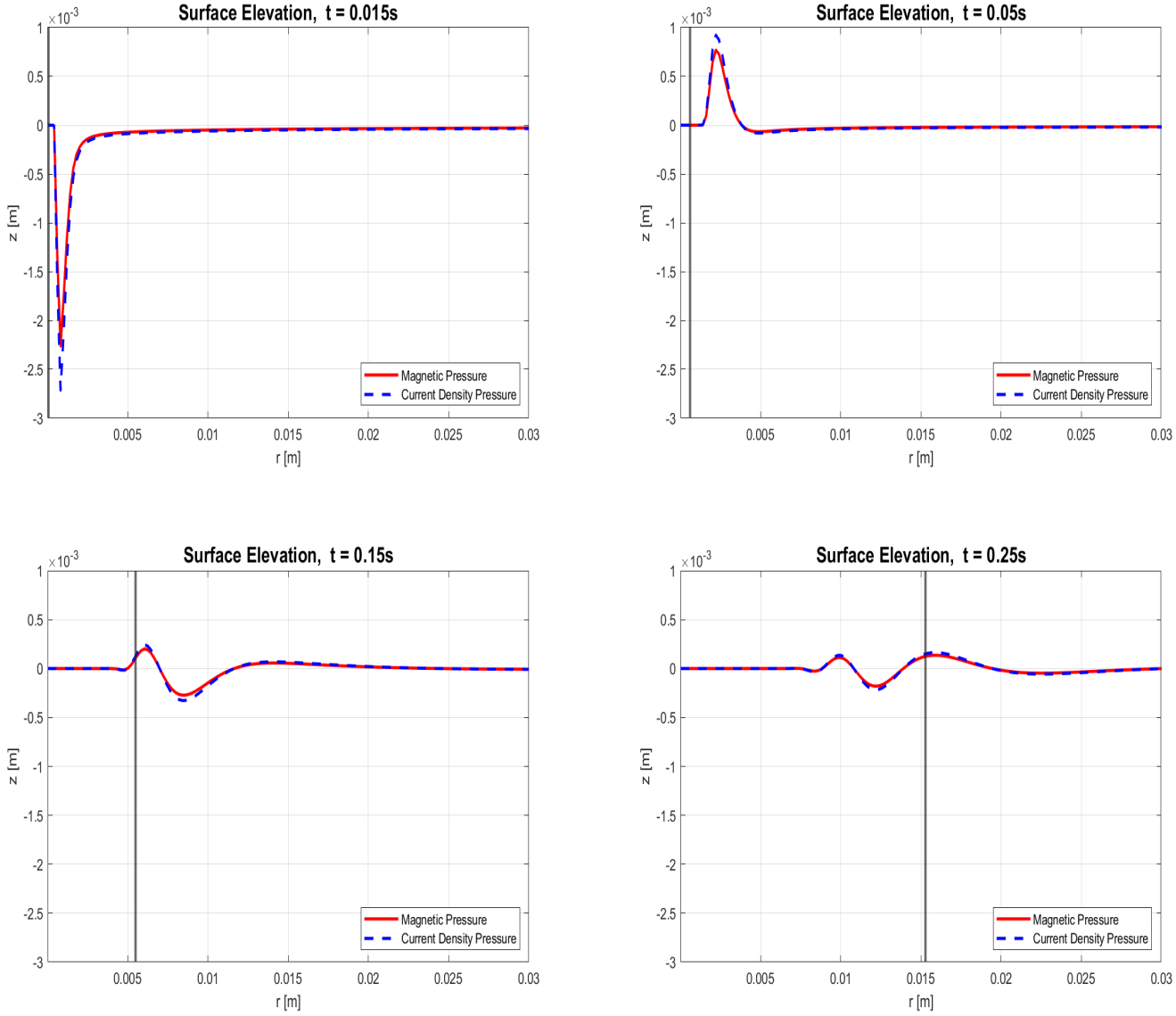

Figure 4.1: Free surface wave propagation predicted with current density and magnetic pressure methods. Solution obtained for input data provided in Table 4.1

4.2 Velocity Analysis

The group velocity of the waveform must be constant to agree with wave mechanics. The group velocity is a packet of a wave that does not break is constant. The leading point of the wave is tracked to find the group velocity. As the leading point progresses outward from the center it becomes a peak, or a trough overtime as seen in Figure 4.1. The velocity of the leading point is found by finding the minimum and maximum value and position of the free surface displacement at every time step.

The position of the maximum and minimum surface displacement is saved at each time step. The velocity of the leading point wave trough is found by taking the difference of the minimum points at each time step.

$$v_{min} = \frac{x_{min}(t_i) - x_{min}(t_{i-1})}{(t_i) - (t_{i-1})} \tag{4.1}$$

The velocity of the leading point for a leading wave trough is

$$v_{min} = 0.4 \ \frac{m}{s} \tag{4.2}$$

The velocity of the leading point while the free surface displacement is positive leading wave is found by taking the difference of the maximum points at each time step.

$$v_{max} = \frac{x_{max}(t_i) - x_{max}(t_{i-1})}{(t_i) - (t_{i-1})} \tag{4.3}$$

The velocity of the leading point for a leading crest is

$$v_{max} = 0.4 \ \frac{\mathrm{m}}{\mathrm{s}} \tag{4.4}$$

The leading point has a consistent group velocity of 0.4 m/s.

4.3 Changing Current

The current applied to the system directly affects both the current density approach and the magnetic pressure approach. Increasing the current increases the initial free surface displacement. The difference in initial surface elevation and subsequent waveform between these approaches is negligible until the current becomes multiple hundreds of kilo-amps.

Table 4.2: Changing Current Input Data

t_0 [μ s]	ω [kHz]	Tin %	Skin Depth [mm]	b Range [mm]	Depth [mm]
50	20	50	4	2.5	10

Table 4.3: Changing Current Values

I_0 [kA]	Magnetic Pressure [mm]	Current Density [mm]	Difference [mm]
50	-0.557	-0.563	0.006
100	-2.226	-2.252	0.026
200	-8.906	-9.008	-0.102

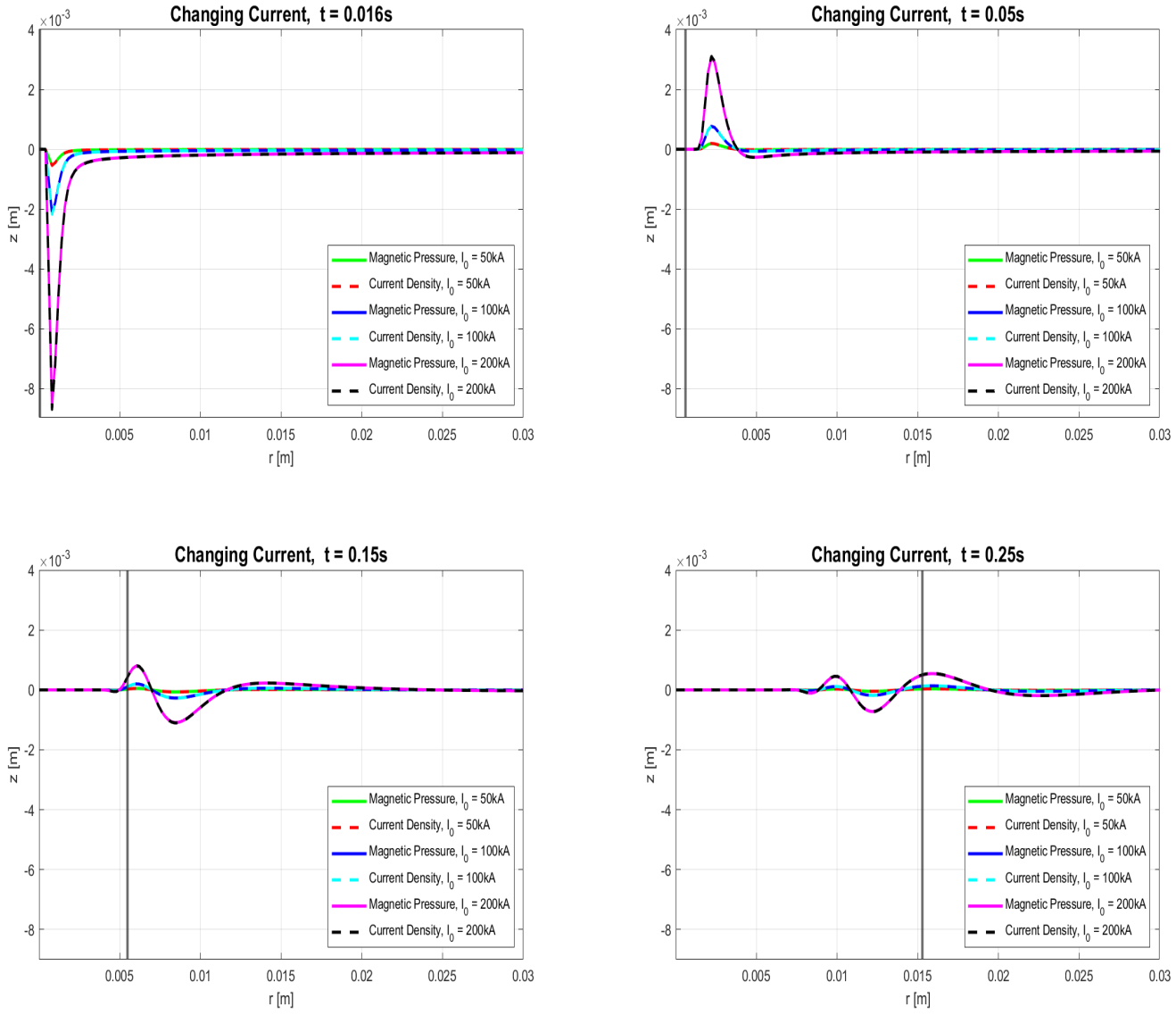

Figure 4.2: Calculated wave propagation of the free surface elevation at different times for a changing current. Increasing the current increases the initial surface displacement.

4.4 Changing Frequency

Changing the frequency used in the analytical solution has a compounding effect on the solution. The frequency is related to the time duration of the current pulse and the skin depth. The longer the time duration increases the time over which the free surface accelerates as given in Equation 2.22. This effect is common to both approaches. The skin depth affects the current density method. The combined increase in skin depth and increase in current pulse duration increases the difference in initial surface elevation and subsequent waveform between the approaches. Conversely, the magnetic pressure approach returns a larger displacement when the frequency is larger, due to the shallower skin depth.

This result highlights the importance of refining the calculation of skin depth.

Table 4.4: Changing Frequency Constant Input Data

I_0 [kA]	Tin %	Depth [mm]	b Range [mm]
100	50	10	3

Table 4.5: Changing Frequency Values

t_0 [μs]	ω [kHz]	Skin Depth [mm]
40	25	3.6
50	20	4
60	17	4.4
Magnetic Pressure [mm]	Current Density [mm]	Difference [mm]
-1.43	-1.3	0.13
-2.24	-2.26	0.02
-3.22	-3.57	0.35

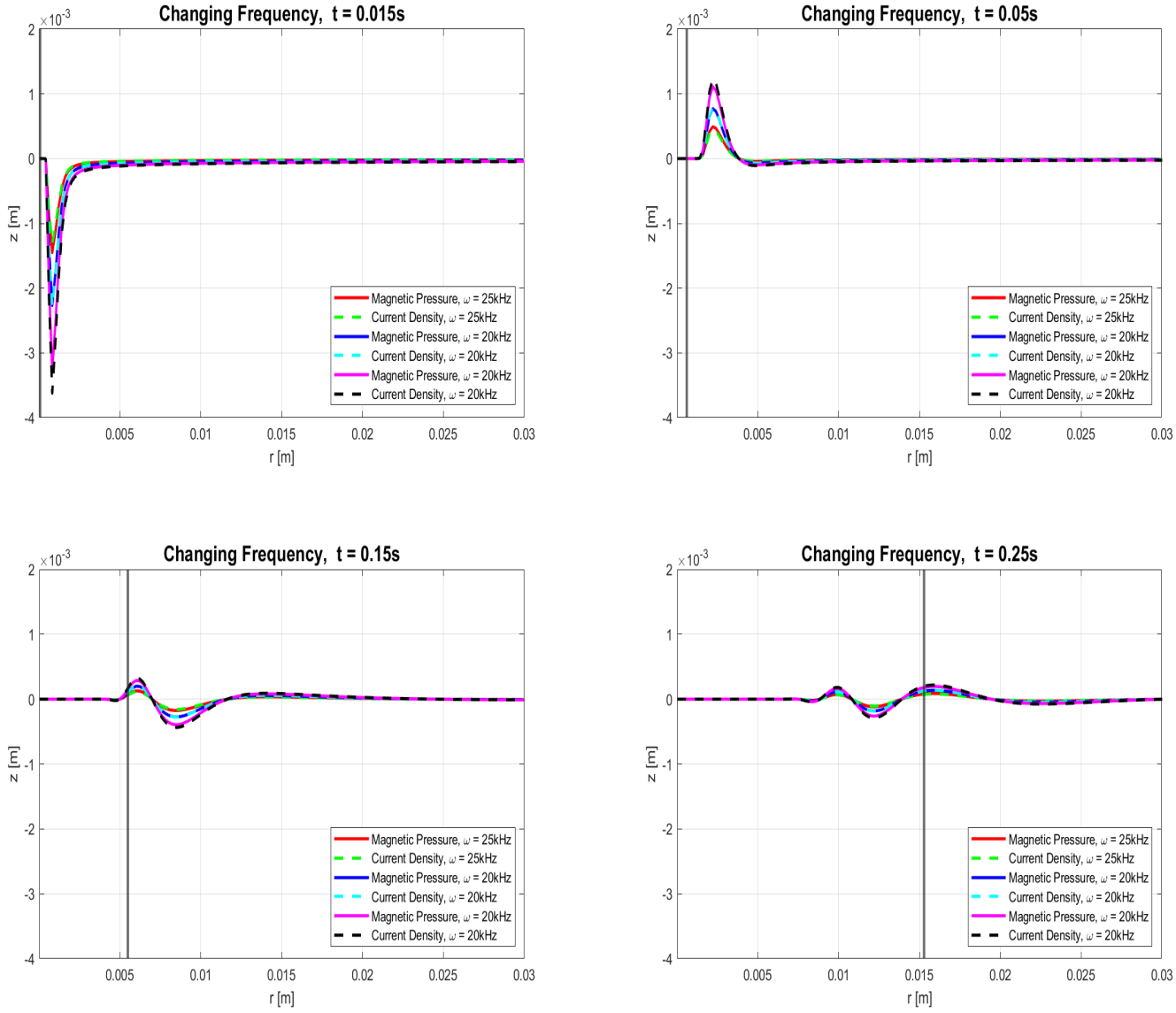

Figure 4.3: Calculated wave propagation of the free surface elevation at different times for a changing frequency. Increasing the current pulse duration increases the initial surface displacement.

4.5 Changing b Range

The b range is the range over which the pressure is applied to the liquid metal free surface. Figure 4.4 shows the difference in initial surface elevation and subsequent waveform between the two methods in relation to changing the b range. Figure 4.1 shows that the pressure in the magnetic pressure method is distributed over a narrow region than the current density method. Closer to the origin, the average pressure exerted by the pressure gradient approach is larger.

An accurate range for the pressure may be determined experimentally.

Table 4.6: Changing b Range Constant Input Data

I_0 [kA]	t_0 [μ s]	ω [kHz]	Tin %	Skin Depth [mm]	Depth [mm]
100	50	20	50	4	10

Table 4.7: Changing b Range Values

b Range [mm]	Magnetic Pressure [mm]	Current Density [mm]	Difference [mm]
1.5	-2.79	-4.45	1.66
2.5	-2.23	-2.25	0.02
5	-0.81	-0.7	0.11

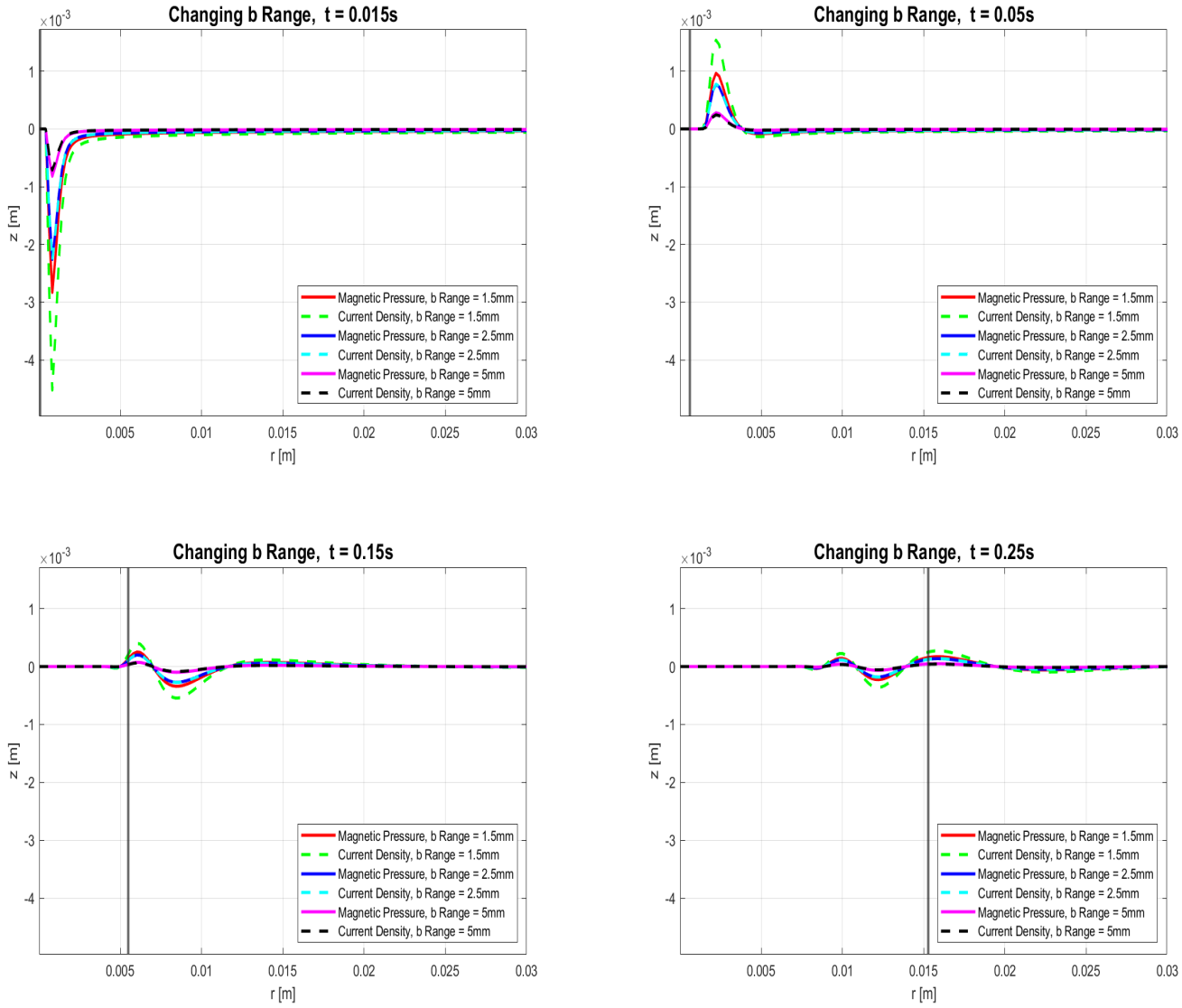

Figure 4.4: Calculated wave propagation of the free surface elevation at different times for a changing b range. Increasing the b range decreases the initial surface displacement.

4.6 Changing Depth

Changing the depth of the liquid metal results in negligible differences between the two approaches. The difference is consistent between the two depths. The difference in initial surface elevation and subsequent waveform between the results appears at later time steps. The general shape of the waveform diverges as time increases.

Table 4.8: Changing Depth Constant Input Data

I_0 [kA]	t_0 [μs]	ω [kHz]	Tin %	Skin Depth [mm]	b Range [mm]
100	50	20	50	4	2.5

Table 4.9: Changing Depth Values

Depth [mm]	Magnetic Pressure [mm]	Current Density [mm]	Difference [mm]
2.5	-2.22639	-2.25209	-0.0257
5	-2.22639	-2.25209	-0.0257
10	-2.22639	-2.25209	-0.0257
15	-2.22639	-2.25209	-0.0257

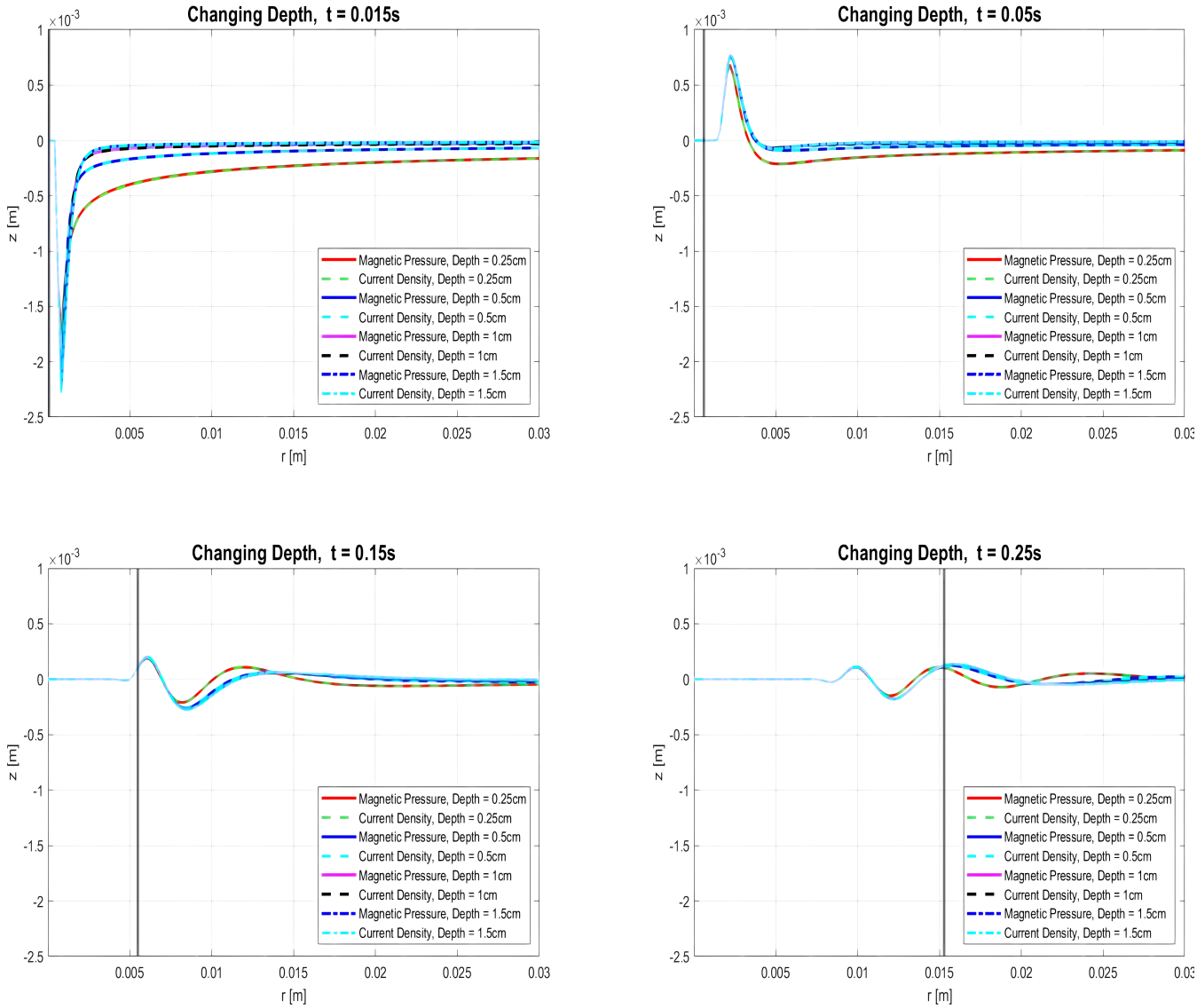

Figure 4.5: Calculated wave propagation of the free surface elevation at different times for changing depth. Increasing the depth of the liquid metal had no effect on the initial free surface displacement.

4.7 Changing Tin Percentage

Changing the percentage of tin in the mixture has a significant impact on the current density method compared to the magnetic pressure method. The magnetic pressure displacement increases with increasing percentages of tin due to the change in density. The changing tin percentage has the opposite effect on the current density approach. The increasing percentage of tin narrows the skin depth, resulting in smaller initial displacements of the free surface. The greatest difference in initial surface elevation and subsequent waveform between the methods occurs when the tin percentage is zero.

Table 4.10: Changing Tin Percentage Constant Input Data

I_0 [kA]	t_0 [μs]	ω [kHz]	Depth [mm]	b Range [mm]
100	50	20	10	2.5

Table 4.11: Changing Tin Percentage Values

Tin %	ρ [kg/m^3]	Skin Depth [mm]
0	10,050	10.2
50	8,520	4
100	6,990	3

Magnetic Pressure [mm]	Current Density [mm]	Difference [mm]
-1.89	-4.86	2.97
-2.23	-2.25	0.02
-2.71	-2.02	0.69

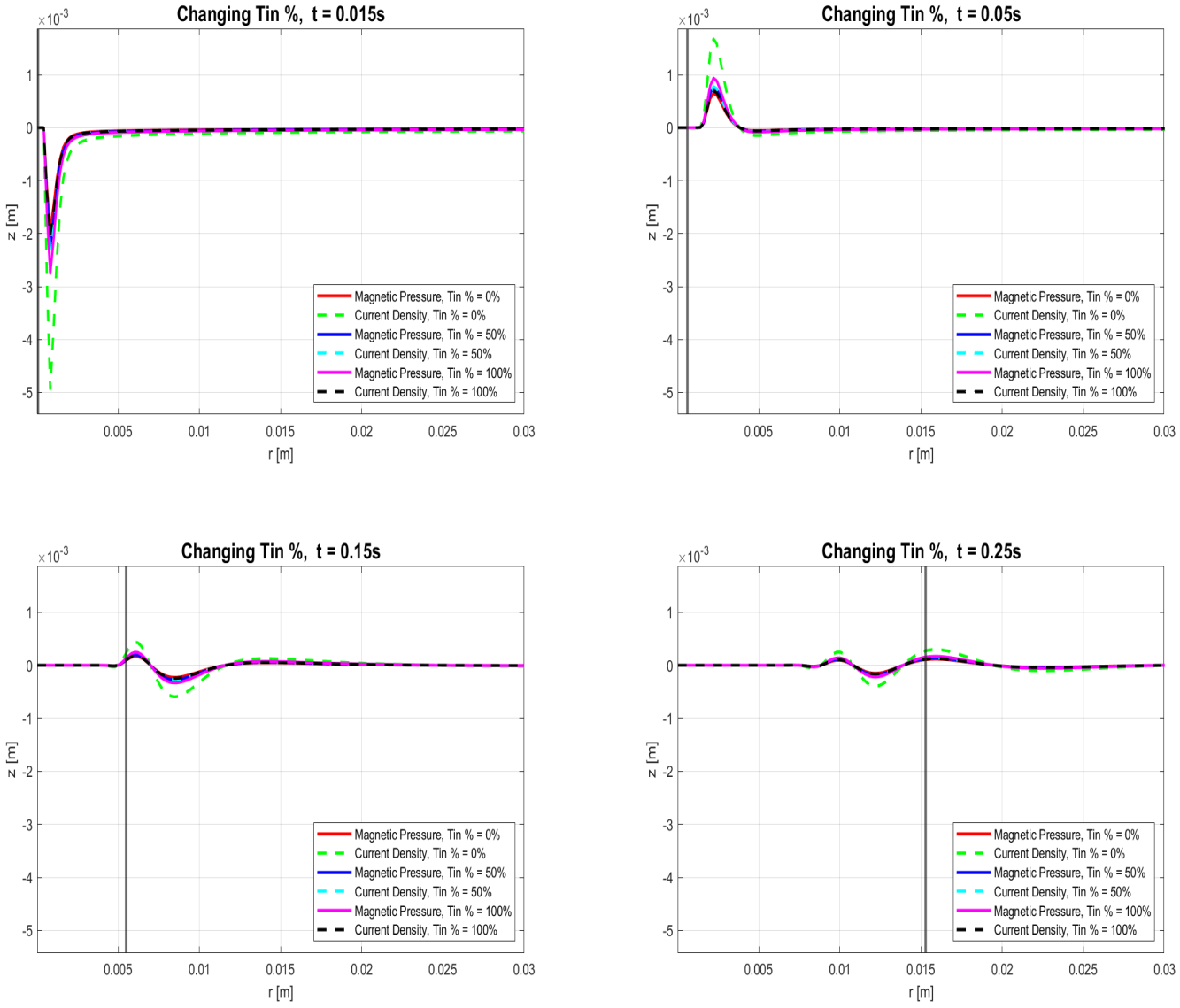

Figure 4.6: Calculated wave propagation of the free surface elevation at different times for changing tin percentage. Increasing the tin percentage increased the magnitude of the initial displacement in the magnetic pressure method. Increasing the tin percentage decreased the magnitude of the initial displacement in the current density approach.

Chapter 5

Verification

STAR-CCM+ is an unsteady RANSE (Reynolds Averaged Naiver Stokes Equation) numerical solver using finite volume method and homogeneous fluid mixture approach on unstructured grids to simulate viscous flow of a liquid of a liquid showing a shape interface with a gas. The solver allows for the modelling of fluid dynamic effects including the initial free surface displacement and the subsequent wave elevation. The CFD solution exploits the axisymmetric effects nature of the Cauchy-Poisson solution to simplify the model and decrease the computation time. The simplified wedge model is shown in Figure 5.1 through Figure 5.3. The narrow point of the wedge is the origin. Using the pressure equation 2.18, applies the pressure from the current density method across the liquid metal free surface. In Figure 5.1 the free surface elevation of the wedge is displaced, and the initial waveform is traveling outward from the origin.

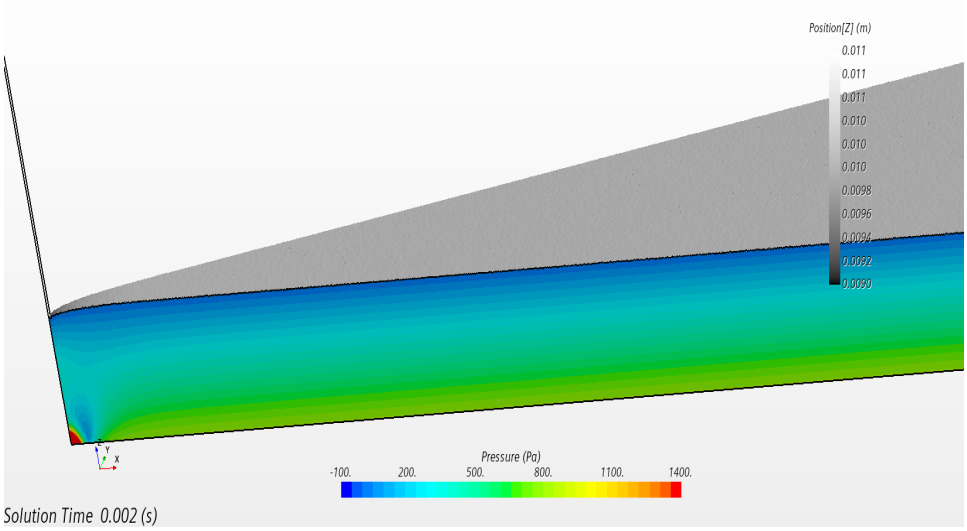

Figure 5.1: Three-dimensional volume of fluid of the wedge used in the CFD solution. The pressure is imparted on the narrow-left side of the wedge. Image occurs at $t = 0.002\ s$.

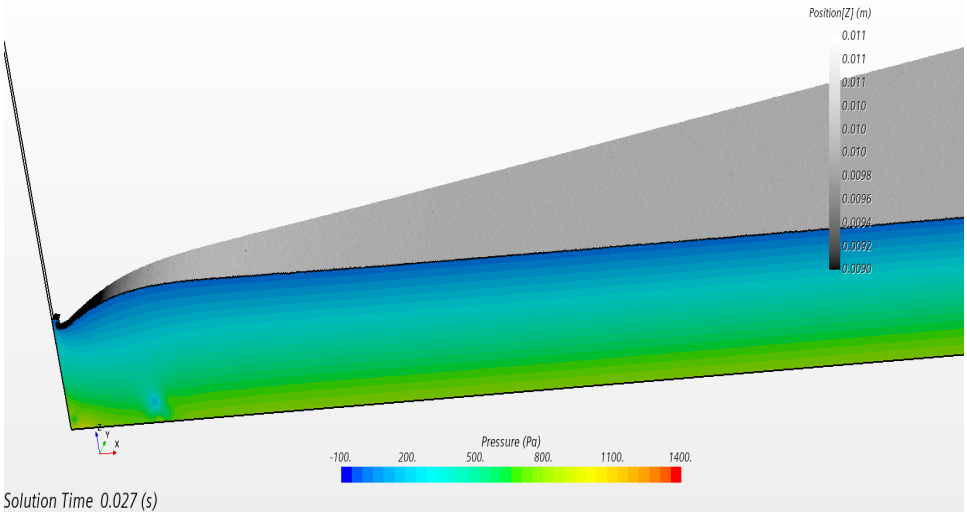

Figure 5.2: Three-dimensional volume of fluid of the wedge used in the CFD solution. The pressure is imparted on the narrow-left side of the wedge. Image occurs at $t = 0.027\ s$.

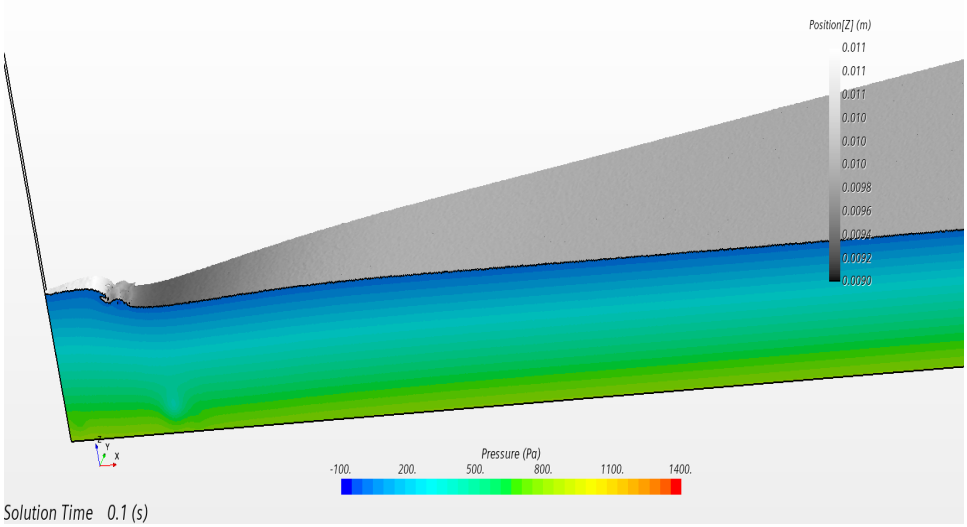

Figure 5.3: Three-dimensional volume of fluid of the wedge used in the CFD solution. The pressure is imparted on the narrow-left side of the wedge. Image occurs at $t = 0.1\ s$.

5.1 CFD Inputs and Outputs

The CFD solution uses five material constants to model the tin-bismuth liquid metal mixture. The material constants are the dynamic viscosity, the molecular weight, the specific heat, the speed of sound and the thermal conductivity. Other components added to the CFD simulation are the equation for the pressure gradient induced by the Lorentz force, Equation 2.18, the skin depth, the current pulse length, and the current magnitude.

Table 5.1: Material Constants Used in CFD Simulation.

	Tin	Bismuth	Average
Dynamic Viscosity [cP]	1.8 [8]	1.56 [9]	1.68
Molecular Weight [u]	118.71	208.98	163.85
Specific Heat [J/(kgK)]	17 [15]	122 [16]	69.5
Speed of Sound [m/s]	2471 [17]	1651 [10]	2061
Thermal Conductivity [W/(mK)]	62.1[15]	7.97 [13]	35.05

The CFD solution calculates the surface displacement from before the current pulse begins. The simulation is initialized with a still-flat free surface. The current density pressure is applied to the free surface during the period of the current pulse causing the surface to depress and generate a waveform. After the current pulse length has elapsed the pressure is removed and the free surface continues to depress for a short amount of time, due to inertia then the wave oscillates, damps, and propagates outward from the point of the wedge.

The results are viewable in multiple ways, with the default functions in CFD, such as 2D and 3D volume fraction, velocity fields and pressure fields. These views are beneficial in quickly discerning the overall nature of the waveform but inadequate for comparing against the simulated results. The CFD simulation outputs a XY.csv file of the discretized waveform at every time step. The file contains the radial position and the surface elevation of the waveform at an individual time step. The surface is identified and tracked at any time, by following the iso-surface corresponding to the volume fraction of the liquid phase. The

number of output files is equal to the number of time iterations. The CFD simulation also outputs a file, t_step.csv, containing the time steps that correspond to the XY.csv displacement files. The time file, t_step.cs, and the radial position-displacement files, XY.csv, constitute a fully descratized solution for the CFD solution.

5.2 Analytical to CFD Results Comparison

Figure 5.4 shows the direct comparison between the CFD solution and the analytical solution using the magnetic pressure method. The initial amplitude of both solutions has a difference of 0.105 mm. The analytical solution oscillates faster than the CFD solution and travels slower.

Table 5.2: Input Data Constants Common to CFD and analytical Solution

I_0 [kA]	t_0 [μ s]	ω [kHz]	Tin %	Skin Depth [mm]	b Range [mm]	Depth [mm]
100	50	20	50	4	2.5	10

Table 5.3: Displacement Values for CFD and analytical Solution

t [s]	Analytical Displacement [mm]	CFD Displacement [mm]	Difference [mm]
0.035	-2.293	-2.188	0.105
0.07	0.771	-1.037	1.808
0.12	0.278	-0.492	0.77
0.169	-0.277	-0.318	0.041

The discontinuity of the CFD solution is due to the breaking of the waveform. Figures 5.5 and 5.6 show the discontinuity of the CFD waveform. The wave-break is a byproduct of the CFD solver not being constrained to the same boundary conditions that the analytical solution is. Equation 3.1 through 3.3 force the free surface to have continuity whereas, CFD model does not. The less constrained free surface allows for the wave to break if the tension forces of the free surface are overcome.

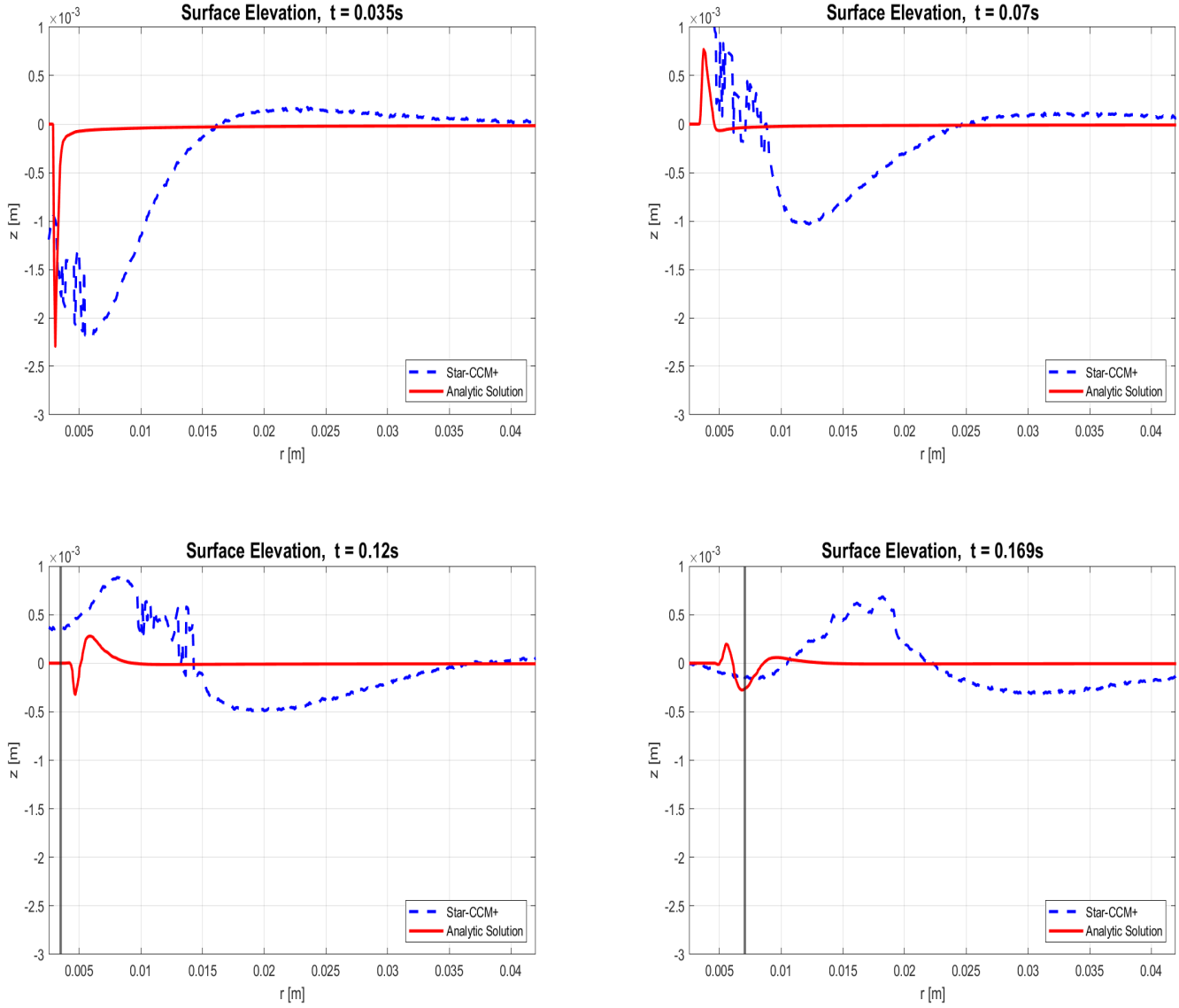

Figure 5.4: Comparison between the analytical and CFD solution. The analytical solution is the solid line. The CFD solution is the dashed line. The initial displacement of both solutions is within 0.1 mm of each other. The analytical solution oscillates faster and travels slower than the CFD solution.

5.3 CFD Velocity

The velocity of the CFD solution is more difficult to find, not only due to the wave break but due the low resolution of the output data. As seen in the second subplot of Figure 5.7,

Figure 5.5: Shades of grey show the fraction of liquid phase in each cell. Black is 100% liquid. White is 0% liquid.

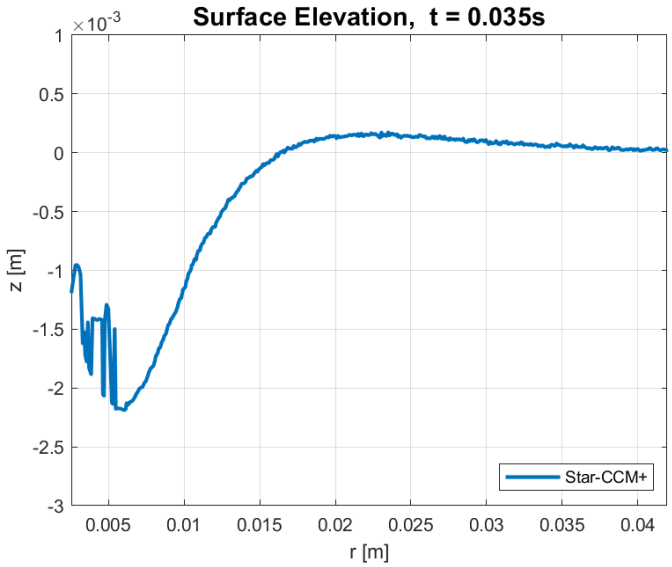

Figure 5.6: Surface elevation predicted by CFD, showing wave-breaking.

the minimum value of the waveform is not as clearly defined as the analytical solution.

The lack of a clear minimum causes the simple velocity calculation for the analytical solution to return a range of answers rather than a consistent one. Finding the velocity of the CFD solution requires more steps than the analytical solution. The initial step for finding the velocity of the CFD solution is the analytical velocity solution. Equation 5.1 finds the velocity of the CFD in the first step.

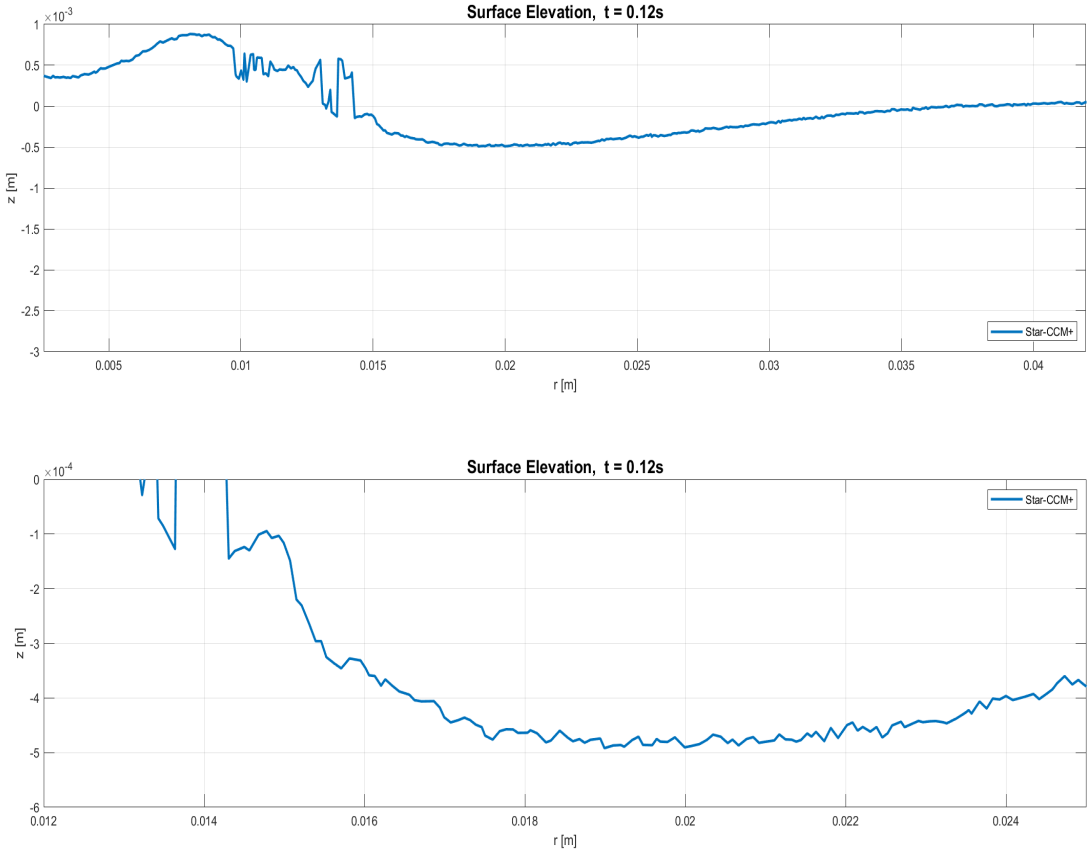

Figure 5.7: Magnified region of the CFD solution. The jagged solution increases the difficulty of finding the CFD solution velocity.

$$v_m in = \frac{x_m in(t_i) - x_m in(t_{i-1})}{t_i - t_{i-1}} \tag{5.1}$$

Then the points where the velocity is negative are removed. These points are non-physical and exist only due to the inconsistent waveform. Then the zero values are removed. The zero values exist where the minimum point does not change between time steps. Then the remaining points are separated into quartiles. The upper and lower quartiles are removed as outliers. The remaining data points are used to find the average, min, max, and median.

Table 5.4: CFD Velocity

t_1 [s]	t_2 [s]	Average v [ms^{-1}]	Max v [ms^{-1}]	Min v [ms^{-1}]	Median v [ms^{-1}]
0.044	0.064	1.758	2.667	1.062	1.883
0.064	0.083	1.714	3.011	0.953	1.531
0.083	0.112	1.876	3.21	0.941	1.726
0.044	0.112	1.796	3.01	0.975	1.717

The time span which returns the most consistent results is between $t = 0.044$ s and $t = 0.112$ s. Before this time, the discontinuities from the wave break are present and after this time the waveform has broadened to the point where the low resolution of the data only returns non-physical results. The average velocity is $v_{avg} = 1.796$ ms^{-1}. This velocity is over four times faster than the analytical solution velocity of 0.4 ms^{-1}.

The difference in wave accuracy between the analytical and CFD methods may be due to the different initial conditions used to initiate the problem. The pressure gradient used to initiate the CFD simulation generates a significant initial fluid mass displacement, which cannot be modeled by the analytical method.

Chapter 6

Conclusion

This thesis presents the analytical solution for the initial free surface displacement of a liquid metal due to an applied pressure. Chapter 2 develops the electromagnetic and kinematic equations used to find the initial free surface displacement of the liquid metal. The kinematic equation uses pressure to find the initial free surface displacement. The two methods for finding the pressure are the magnetic pressure method and the current density method. Chapter 4 details the analytical solution over a range of pressures and the two pressure methods. In Chapter 5 the CFD model, solved by an unsteady multi-phase RANSE solver, is used to verify the accuracy of the analytical solution. Chapter 5 compares the CFD solution against the magnetic pressure method of the analytical solution.

6.1 Summary of Results

The analytical solution presented in this thesis predicts the initial surface displacement of a liquid metal free surface due to an imparted pressure. The analytical solution can be calculated over a range of variables including the electric current, the current pulse length, the range of the applied pressure, b range, the percentage of tin, and the depth of the liquid metal. The analytical solution also presents two methods for calculating the pressure. One method uses the magnetic pressure, and the other method uses the current density to determine the pressure. The difference in initial surface elevation between the two methods

is 0.44 mm and is presented in Table 2.4. The analytical solution is compared with the CFD solution in Chapter 5. The difference in initial surface elevation between the analytical solution and the CFD solution is 0.1 mm. After the initial displacement the agreement between the solutions breaks. The magnitude of the displacement and the shape of the waveform quickly diverge. The differences between the analytical and CFD methods may be due to differences in the initial conditions used to initiate the problem.

6.2 Improvements

The improvements of the electrodynamic components of the analytical solution are mainly concerned with the derivation of the skin depth, the liquid metal current density, and the magnetic field penetration of the liquid metal. Improving these calculations will create a more complete understanding of the system and improve further work. The main step to improving the skin depth calculation should be to find more accurate values for the liquid metal mixture's material properties. This thesis presents simple averages of the material properties of tin and bismuth. Combining metals, or any elements, seldom results in the properties chemical and material properties simply averaging. Improving the skin depth calculation directly impacts the liquid metal current density calculation. The skin depth determines the depth with which the current from the wire dissipates in the liquid metal. Improving the accuracy of the material properties in the liquid metal mixture impacts both the current density method and the magnetic pressure method. Figure 4.6 in section 4.7, the changing tin percentage section shows the impact of changing the material properties for both methods.

Improvements to the liquid metal current density are more involved than the improvements to the skin depth. Improving the current density within the liquid metal involves finding

a more accurate path for the current. Figure 2.7 shows the simplified path for the current density in the liquid metal. An unrestricted current density is free to move in more than one direction. The unrestricted current density may more in any combination of r theta or z. The additional degrees of freedom of the current density combined with the magnetic field will create pressure forces in more than just the z direction. The current density components that travel in both the r and z direction will generate a pressure in the azimuthal direction. The azimuthal pressure will cause the liquid metal tangential to the radial direction. In general terms, the azimuthal pressure will generate a wave that moves outward in a spiral.

The magnetic field in this thesis penetrated the entire liquid metal. The constant magnitude of the magnetic field throughout the liquid metal allowed for the use of the current density method. The pressure found in the current density method relies upon the cross product of the current density and the magnetic field. The magnetic field in the analytical solution penetrates uniformly as a constant value. Determining an accurate method for the magnetic field penetration will improve the analytical solution.

The kinematic equations may be improved by incorporating a method for the continued motion of the liquid metal due to inertia. The analytical solutions currently consider the motion of the accelerated mass during the current pulse length. The initial free surface displacement used in the analytical solution is the displacement of the liquid metal when the current pulse ends. This initial free surface displacement is non-physical as the displacement will continue due to inertia.

There are two improvements to the fluid components of the analytical solution. The first fluid improvement is a more accurate initial free surface displacement equation. There may be a more accurate initial equation. The initial free surface displacement equation used in the analytical solution does not demonstrate the broadness of the CFD solution used in Chapter 5.

The second improvement of the analytical solution is the inclusion of a repeated pulse. The Z-pinch that the LEX generates fusion events in a brief 50 μs period. The pulse repeats multiple times during the device's operation. The repeated pulse improvement will determine the behavior of the liquid metal under repeated pressure pulses. Under repeated pressure pulses the liquid metal may exhibit a constructive of destructive waveform. The constructive waveform will increase the amplitude of the free surface displacement. The destructive waveform will decrease the amplitude of the free surface displacement.

The improvements to the CFD solution involve finding more accurate values for the material constants and the fidelity of the free surface mesh. The values of the material constants were simply averaged, and more accurate values will improve the accuracy of the solution. Improving the fidelity of the liquid metal free surface mesh will also improve the accuracy of the verification. The accuracy of the maximum free surface displacement will remain the same. The accuracy of the velocity will improve.

Appendices

Appendix A

One of the most common methods to achieve fusion has been between Deuterium-Tritium. The reactants are two isotopes of hydrogen. The deuterium isotopes nucleus consists of a proton and a neutron. The tritium isotope's nucleus consists of a proton and two neutrons. Deuterium's natural abundance is approximately 1 in 6420 that of hydrogens, and it is stable in contrast, tritium is unstable, with a half-life of 12.5 years. This results in only trace amounts of tritium being found on Earth. Tritium needs to be produced artificially, and its production is a research subject of its own. The fusion of these isotopes results in the formation of a helium nucleus, a neutron, and a total of 17.6 MeV of energy created per reaction, as given below in equation A.1. The goal of fusion is to convert the 17.6 MeV into electricity via steam or other methods.

$$ {}^{2}_{1}D + {}^{3}_{1}T \rightarrow {}^{4}_{2}He(3.5\text{MeV}) + {}^{1}_{0}n(14.1\text{MeV}). \tag{A.1} $$

The energy density calculations begin with the summation of the mass of the reactants.

$$ m = 2.014u + 3.016u = 5.032 \ \frac{\text{u}}{\text{reaction}} \tag{A.2} $$

Now taking the standard mass of fuel used in energy comparisons, 1kg, the to determine the number of moles of fuel per kilogram

$$ \text{moles} = \frac{1\text{kg}}{5.032\text{g mol}^{-1}} = 198.8 \text{ moles} \tag{A.3} $$

Multiplying the number of moles by Avogadro's number gives the total number of reactions per kilogram of fuel.

$$\text{Reactions} = 198.8\text{moles} * 6.02 \times 10^{23} \ \frac{\text{reaction}}{\text{moles}} = 1.974 \ \times 10^{26} \text{ reactions} \tag{A.4}$$

To find the energy, multiply the number of reactions per kilogram by the amount of energy released per kilogram, 17.6 MeV, and convert from electron volts to mega joules

$$E = (1.974 \times 10^{26}\text{reaction})(17.6\text{MeV/reaction})(1.602 \times 10^{-13}\text{J/MeV}) = 3.37 \times 10^{7}\text{MJ/kg} \tag{A.5}$$

A.1 Nuclear Fission Stoichiometry

The most common fission method involves Uranium-235 and occurs when one absorbs a neutron turning the U-235 into unstable U-236. This unstable isotope quickly decays into Krypton-92, Barium-141, and these neutrons. In total, each reaction generates 202 MeV of energy. In controlled fusion, three neutrons released will be absorbed into other U-235's repeating the process and generating electricity by steam production. The nuclear stoichiometric equations begin in the same way as in nuclear fusion with equation A.6.

$$^{235}U + n \rightarrow ^{141} Ba + ^{92} Kr + 3n \tag{A.6}$$

The energy density calculations begin with the summation of the mass of the reactants.

$$\text{m} = 235u + 1u = 236 \frac{\text{u}}{\text{reaction}} \tag{A.7}$$

Taking the standard mass of fuel used in energy comparisons, 1 kg, to determine the number of moles of fuel per kilogram

$$\text{moles} = \frac{1 \text{ kg}}{236\text{g mol}^{-1}} = 4.24 \text{ mol.} \tag{A.8}$$

Multiplying the number of moles by Avogadro's number gives the total number of reactions per kilogram of fuel

$$\text{Reactions} = 4.24 \text{ mol} \times 6.02 \times 10^{23} \frac{\text{reaction}}{\text{mol}} = 2.54 \times 10^{24} \text{ reactions} \tag{A.9}$$

To find the energy, multiply the number of reactions per kilogram by the amount of energy released per kilogram, 202 MeV, and convert from electron volts to mega joules.

$$E = \left(2.54 \times 10^{24} \text{ reactions}\right) \left(202 \frac{\text{MeV}}{\text{reaction}}\right) \left(1.602^{-13} \frac{\text{J}}{\text{MeV}}\right) = 8.24 \times 10^{6} \frac{\text{MJ}}{\text{kg}} \tag{A.10}$$

A.2 Methane Stoichiometry

Due to methane energy production consisting of a chemical reaction instead of a nuclear one, the energy calculation involves the first law of thermodynamics. The idealized thermodynamic system used in methane energy calculations require constant volume, and no kinetic or potential energy changes within the system. The result is only that maximal amount of energy is released per reaction. Starting with the stoichiometry equation for methane, equation A.11

$$CH_4 + 2(O_2 + 3.76N_2) \rightarrow CO_2 + 2H_2O + 7.52N_2 \tag{A.11}$$

To calculate the energy produced in a chemical process the enthalpy of combustion equation

is required. The enthalpy of combustion equations utilizes the known values of energy per kmol of various substances. Within these equations a negative sign indicates an exothermic reaction. The heat is generated during the creation of the products given on the right hand side of the stoichiometric equation given above.

$$\begin{aligned} Q_{cv} &= 1CO_2(g) + 2H_2O(l) - 1CH_4(g) \\ &= 1(-393,520 \text{ kJ/kmol}) + 2(-285,820 \text{ kJ/kmol}) - 1(-74,850 \text{ kJ/kmol}) \\ Q_{cv} &= -890,310 \text{ kJ/kmol} \end{aligned} \tag{A.12}$$

The last step is to convert the result of A.13 into energy density.

$$\begin{aligned} q_{cv} = \left[\frac{Q_{cv}}{M_{CH_4}}\right] &= \frac{-890,310}{(12+4)} \\ &= -55.6 \text{ MJ/kg} \end{aligned} \tag{A.13}$$

q_{cv} is the enthalpy of combustion per unit mass of methane.

A.3 Stationary Phase Approximation

As stated previously the solutions presented here are not analytically solvable and are thus not entirely enlightening on their own. To make use of them, we apply the stationary phase approximation to them. The purpose of the stationary phase method is to simplify systems by taking the phase of sinusoids into account. If sinusoids are found to have the same phase, they add together constructively. If they are found to have different phases, they are found to be destructive.

The stationary phase approximation works to simplify the system by finding a point where

the system is stationary. The stationary point is found by adding the constructive and destructive components. This results in a non-integral solution that may be solved analytically. The steps to the approximation are detailed as follows:

$$I(\lambda) = \int_a^b f(t)e^{i\lambda g(t)}dt \tag{A.14}$$

. Where

$$g'(c) = 0, \quad \mu g''(c) = |g''(c)| \tag{A.15}$$

Applying these gives

$$I(\lambda) = e^{i\lambda g(c)} \int_a^b f(t)e^{i\lambda[g(t)-g(c)]}dt \tag{A.16}$$

The Coales-Euler formula $e^{i\lambda[g(t)-g(c)]}$ is highly oscillatory for $t \neq c$ and $\lambda > 1$

$$I(\lambda) \approx e^{i\lambda g(c)} \int_{c-\epsilon}^{c+\epsilon} f(t)e^{i\lambda[g(t)-g(c)]}dt \tag{A.17}$$

$$\approx f(c)e^{i\lambda g(c)} \int_{c-\epsilon}^{c+\epsilon} e^{i\lambda/2g''(c)(t-c)^2}dt \tag{A.18}$$

$$\approx f(c)e^{i\lambda g(c)} \int_{-\infty}^{\infty} e^{i\lambda/2g''(c)(t-c)^2}dt \tag{A.19}$$

$$\approx f(c)e^{i\lambda g(c)} \int_{-\infty}^{\infty} e^{i\lambda/2g''(c)s^2}ds \tag{A.20}$$

$$= f(c)e^{i\lambda g(c)} \sqrt{\frac{2\pi i}{\lambda g''(c)}} \tag{A.21}$$

$$= f(c)e^{i\lambda g(c)}\sqrt{\frac{2\pi}{\lambda|g''(c)|}}(i\mu)^{1/2} \tag{A.22}$$

$$= f(c)e^{i\lambda g(c)}\sqrt{\frac{2\pi}{\lambda|g''(c)|}}e^{\pi i\mu/4} \quad \text{for } \lambda >> 1 \tag{A.23}$$

Which to leading order gives

$$I(\lambda) \sim f(c)e^{i\lambda g(c)}\sqrt{\frac{2\pi}{\lambda|g''(c)|}}e^{\pi i\mu/4} \quad \text{for } \lambda \to \infty \tag{A.24}$$

Bibliography

[1] Dan Weber, Prototype Images

[2] Lokenath Debnath, 1994, *Nonlinear Water Waves*, Academic Press,

[3] M. A. Guzachev; N. Yu. Konstantinova; P. S. Popel; . G. Mozgovoy, 2011, "Temperature dependences of kinematic viscosity of bismuth, lead, and their mutual solutions", Thermophysics and Aeromechanics, **18**(3), pp 469-475

[4] E. V. Rozhitsinaa, S. Grunerb, I. Kabanb, W. Hoyerb, V. E. Sidorova, and P. S. Popel, 2011r "Dynamic Viscosities of Pure Tin and Sn–Ag, Sn–Cu, and Sn–Ag–Cu Eutectic Melts", Ural State Pedagogical University Ekaterinburg

[5] A.M. Chebotarev, 1974, "The method of stationary phase for non-differentiable functions", USSR Computational Mathematics and Mathematical Physics , **14** (14), pp 210–214

[6] David J. Griffiths, 1999, *Introduction to Electrodynamics, 3rd ed*, Prentice Hall.

[7] Chen, Francis F, 2015, *Introduction to Plasma Physics and Controlled Fusion*, Springer,

[8] E. V. Rozhitsina, S. Gruner, I. Kaban, W. Hoyer, V. E. Sidorov, and P. S. Popel, 2009, "Dynamic Viscosities of Pure Tin and Sn–Ag, Sn–Cu, and Sn–Ag–Cu Eutectic Melts", Ural State Pedagogical University, Ekaterinburg, Russia.

[9] M.A. Guzachev, N.Yu. Konstantinova, P.S. Popel, and A.G. Mozgovoy, 2010, "Temperature dependences of kinematic viscosity of bismuth, lead, and their mutual solutions", Ural State Pedagogical University, Ekaterinburg, Russia.

[10] David R. Lide, 2003, *CRC Handbook of Chemistry and Physics, 84th Edition*, CRC Press.

[11] Jorge Garza-Ulloa, 2019, "Research: Electromagnetic Field Toroidal And Magnetic Confinement Fusion Tokamak", University of Texas, El Paso.

[12] Dr. C Grisolia, 2007, "Plasma Wall Interactions in Tokamak", Association Euratom-CEA.

[13] Vitaly Sobolev, 2011, "Database of Thermophysical Properties of Liquid Metal Coolants for GEN-IV", Belgian Nuclear Research Centre.

[14] U. Shumlak, J. Chadney, R.P. Golingo, D.J. Den Hartog, M.C. Hughes, S.D. Knecht, B.A. Nelson, W. Lowrie, R.J. Oberto, M.P. Ross, J.L. Rohrbach, and G.V. Vogman, 2011, "The Sheared Flow Stabilized Z-Pinch", Aerospace Energetics Research Program, University of Washington, Seattle, USA .

[15] "Thermal Properties of Metals, Conductivity, Thermal Expansion, Specific Heat", https://www.engineersedge.com/properties_of_metals.htm

[16] "Bismuth - Specific Heat, Latent Heat of Fusion, Latent Heat of Vaporization", https://www.nuclear-power.com/bismuth-specific-heat-latent-heat-vaporization-fusion/

[17] "Sound Speeds in Water, Liquid and Materials", https://www.rshydro.co.uk/sound-speeds/

[18] 2019, "Background: Radioactive Waste", https://www.nrc.gov/docs/ML0501/ML050110277.pdf

[19] Steve Fetter, E.T. Cheng, F.M. Mann, 1988, "Long-term radioactivity in fusion reactors", Fusion Engineering and Design, **6**, pp 123-130